The conserved AAA-ATPase PCH-2 distributes its regulation of meiotic prophase events by remodeling multiple meiotic HORMADs in *C. elegans*

Anna E. Russo*, Stefani Giacopazzi*, Alison Deshong*, Malaika Menon*, Valery Ortiz*, Kaori M. Ego#, Kevin D. Corbett# and Needhi Bhalla*[1]

* Department of Molecular, Cell and Developmental Biology, University of California, Santa Cruz, Santa Cruz, CA 95064

Department of Cellular and Molecular Medicine, University of California, San Diego, La Jolla, CA 92093

[1] corresponding author: nbhalla@ucsc.edu
Department of Molecular, Cell and Developmental Biology
225 Sinsheimer Labs
University of California, Santa Cruz
Santa Cruz, CA 95064
phone: (831) 459-1319
fax: (831) 459-3139

Abstract

During meiotic prophase, the essential events of pairing, synapsis, and recombination are coordinated with meiotic progression to promote fidelity and prevent aneuploidy. The conserved AAA+ ATPase PCH-2 controls a variety of chromosome behaviors, including coordinating pairing, synapsis and recombination between homologous chromosomes to guarantee crossover assurance and accurate chromosome segregation. However, how PCH-2 accomplishes this coordination is poorly understood. Here, we use a combination of genetic, cytological, and biochemical analyses to show that PCH-2 regulates pairing, synapsis and recombination in *C. elegans* by remodeling meiotic HORMADs from a closed conformation to an unlocked conformation. Further, we find PCH-2 coordinates these events by distributing this regulation among the three essential meiotic HORMADs in *C. elegans*: PCH-2 acts through HTP-3 to regulate pairing and synapsis, HIM-3 to promote crossover assurance, and HTP-1 to control meiotic progression. In addition to identifying a molecular mechanism for how PCH-2 regulates interhomolog interactions, our results provide a possible explanation for the expansion of this family as a conserved evolutionary feature of meiosis. Taken together, our work demonstrates that PCH-2's well-characterized role in remodeling mitotic HORMADs applies to meiotic HORMADs and this remodeling coordinates homolog pairing, synapsis, recombination and meiotic progression to ensure accurate meiotic chromosome segregation.

48 **Introduction**

49 All sexually reproducing organisms depend on the specialized cell division called meiosis, which
50 produces haploid gametes such as sperm, eggs, and pollen. During meiosis, cells combine one
51 round of DNA replication with two rounds of chromosome segregation, all of which is tightly
52 regulated to ensure that gametes inherit the correct number of chromosomes. Errors in meiosis
53 can lead to aneuploid gametes that cause infertility, birth defects and miscarriages (Hassold &
54 Hunt, 2001). Therefore, understanding how meiotic events are coordinated has important
55 implications for reproductive health.

56

57 During prophase I of meiosis, chromosome pairs or homologs undergo a series of events known
58 as pairing, synapsis, and crossover recombination. First, homologs find each other and pair
59 within the nucleus. Next, a molecular structure called the synaptonemal complex (SC)
60 assembles between homologs and stabilizes homolog pairing in a process called synapsis.
61 Finally, homologs undergo crossover recombination, which serves two important purposes.
62 First, it shuffles alleles to create new genetic combinations that can be acted upon by natural
63 selection. Second, it physically links homolog pairs, which is required for homologs to properly
64 remodel, orient on the spindle, and segregate correctly during the first meiotic division.

65

66 Despite being described as a linear pathway, the processes of pairing, synapsis and
67 recombination between homologous chromosomes are highly dynamic and can occur
68 simultaneously, requiring active coordination. Further, these events can also initiate
69 inappropriately between non-homologous chromosomes and therefore need to be corrected.
70 We have shown that the highly conserved AAA+ ATPase, Pachytene checkpoint 2 (PCH-2),
71 contributes to both this coordination and correction (Deshong, Ye, Lamelza, & Bhalla, 2014;
72 Giacopazzi, Vong, Devigne, & Bhalla, 2020). However, how it carries out these roles is currently
73 unclear.

74 PCH-2 has been shown to act through a family of proteins that contain a HORMA domain
75 (HORMAD proteins) to mediate a variety of chromosome behaviors, including meiotic
76 interhomolog interactions. HORMADs were named after the first proteins in this family to be
77 discovered in budding yeast: Hop1, Rev7, and Mad2 (Aravind & Koonin, 1998) and meiotic
78 HORMADs are essential to structure meiotic chromosomes for the meiosis-specific events of
79 homolog pairing, synapsis, and recombination (Ur & Corbett, 2021). Despite having essential
80 roles in meiotic prophase, meiotic HORMADs differ greatly across eukaryotes in the number of
81 family members they contain. For example, *S. cerevisiae* and *S. pombe* each have one meiotic
82 HORMAD (Hollingsworth, Goetsch, & Byers, 1990; Lorenz et al., 2004), mice and *Arabidopsis*
83 have two (Caryl, Armstrong, Jones, & Franklin, 2000; Fukuda, Daniel, Wojtasz, Toth, & Hoog,
84 2010; Wojtasz et al., 2009) and *C. elegans* has four (Couteau & Zetka, 2005; Goodyer et al.,
85 2008; Martinez-Perez & Villeneuve, 2005; Zetka, Kawasaki, Strome, & Muller, 1999). In both
86 mice and plants, one meiotic HORMAD plays a more integral role in the events of pairing,
87 synapsis, and recombination, indicating some separation of function (Caryl et al., 2000; Daniel
88 et al., 2011; Kogo, Tsutsumi, Ohye, et al., 2012; Shin et al., 2010; Wojtasz et al., 2012; Wojtasz
89 et al., 2009). This separation of function is also observed in *C. elegans* among the three
90 essential HORMADs (Kim et al., 2014b): HTP-3 is responsible for double strand break formation
91 (Goodyer et al., 2008) and REC-8-mediated sister chromatid cohesion (Severson, Ling, van
92 Zuylen, & Meyer, 2009); HIM-3 promotes synapsis (Kim et al., 2014b) and homolog access to
93 ensure repair off the homolog versus the sister chromatid during crossover recombination
94 (Couteau, Nabeshima, Villeneuve, & Zetka, 2004); and HTP-1, in addition to contributing to
95 homolog access along with HIM-3, also controls the timely initiation of SC assembly once
96 homologs are paired properly (Couteau & Zetka, 2005; Martinez-Perez & Villeneuve, 2005) and
97 the protection of sister chromatid cohesion during the first meiotic division (Martinez-Perez et
98 al., 2008). The fourth meiotic HORMAD, HTP-2, is not essential and is largely redundant with
99 HTP-1 (Couteau & Zetka, 2005; Martinez-Perez et al., 2008).

100 HORMAD proteins have a characteristic N-terminal HORMA domain that allows HORMADs to
101 adopt two different conformations: a closed conformation and an open/unlocked conformation
102 (reviewed in (Rosenberg & Corbett, 2015)). In the closed conformation, a peptide on a binding
103 partner called the “closure motif” binds the core of the HORMAD’s HORMA domain. This
104 interaction is further stabilized by a C-terminal region of the HORMA domain called the safety
105 belt, which wraps around the HORMAD to lock in the binding partner’s closure motif against the
106 HORMA domain core. Conversion of the HORMAD from the closed to open conformation
107 occurs when the binding partner’s closure motif is displaced, and the safety belt region of the
108 HORMA domain rearranges to occupy the closure motif interaction site. Biochemical and
109 structural studies show that PCH-2 is directly responsible for the conversion of closed
110 conformers to open conformers for the mitotic HORMADs Mad2 (Ye et al., 2015) and Rev7
111 (Clairmont et al., 2020), where this remodeling relies on a direct interaction between PCH-2 and
112 the N-terminus of the HORMAD (Alfieri, Chang, & Barford, 2018; Ye et al., 2017).
113
114 This conformational switching is also essential for meiotic HORMAD function. Closed versions
115 of meiotic HORMADs assemble on meiotic chromosomes to drive pairing, synapsis,
116 recombination, and meiotic progression (Kim, Kostow, & Dernburg, 2015; Kim et al., 2014b).
117 Instead of adopting an open conformation, meiotic HORMADs adopt an intermediate “extended”
118 state that has been referred to as unlocked or unbuckled (West, Komives, & Corbett, 2017). The
119 physiological relevance of unlocked meiotic HORMADs *in vivo* is unclear.
120
121 While studies with other HORMADs, such as Mad2 and Rev7, provide a powerful framework to
122 imagine PCH-2’s molecular mechanism during meiotic prophase, identifying PCH-2’s specific
123 role during meiosis has been challenging. In contrast to Mad2 and Rev7, attempts to undertake
124 similar structural and biochemical analysis of PCH-2 and meiotic HORMADs have been less
125 informative. However, prior evidence from budding yeast, plants, and mammals indicates that

126 PCH-2 binds and acts directly on meiotic HORMADs. In budding yeast, Pch2 has been shown
127 to bind to and remodel meiotic HORMADs *in vitro* (Chen, Jomaa, Ortega, & Alani, 2014).
128 Additionally, PCH-2's orthologs in other systems have been shown to promote meiotic
129 progression (Raina & Vader, 2020b) by removing or redistributing meiotic HORMADs from
130 chromosome axes upon synapsis, including budding yeast (Borner, Barot, & Kleckner, 2008;
131 Joshi, Barot, Jamison, & Borner, 2009), *Arabidopsis* (Lambing et al., 2015) and mice (Wojtasz
132 et al., 2009). In mice, the removal of the meiotic HORMAD, HORMAD1, at the onset of synapsis
133 is abolished in both TRIP13 mutants (Wojtasz et al., 2009) or when the N-terminus of
134 HORMAD1 is deleted (Ye et al., 2017), indicating that PCH-2 and its orthologs' remodeling of
135 meiotic HORMADs is similar to its remodeling of Mad2 and Rev7. However, meiotic HORMADs
136 are not removed from chromosomes upon synapsis in all systems, such as in *C. elegans*
137 (Couteau et al., 2004; Couteau & Zetka, 2005; Goodyer et al., 2008; Martinez-Perez &
138 Villeneuve, 2005). Further, PCH-2 and its orthologs localize to meiotic chromosomes prior to
139 synapsis in budding yeast, plants and *C. elegans* (Cuacos et al., 2021; Deshong et al., 2014;
140 Joshi et al., 2009; Lambing et al., 2015; San-Segundo & Roeder, 1999). These data raise the
141 important question of whether remodeling of meiotic HORMADs plays additional roles during
142 meiotic prophase.
143
144 Here, we use a combination of genetic, cytological and biochemical data to demonstrate that
145 PCH-2 remodels meiotic HORMADs to regulate and coordinate pairing, synapsis, crossover
146 recombination, and meiotic progression in *C. elegans*. We show that a missense mutation in the
147 HORMA domain of HTP-3 suppresses pairing and synapsis defects in *pch-2* mutants but
148 exacerbates its recombination defects, indicating these two proteins cooperate to promote
149 pairing and synapsis but regulate recombination independently. We also show that a similar
150 mutation in *him-3* exacerbates synapsis defects in *pch-2* mutants but suppresses its
151 recombination defects, suggesting that PCH-2 acts on HIM-3 specifically to promote crossover

152 recombination. Finally, we show that corresponding mutations in the meiotic HORMAD HTP-1
153 produce a delay in meiotic progression, with consequences for synapsis and recombination, and
154 can be partially suppressed by a mutation in *pch-2*, suggesting that PCH-2 cooperates with
155 HTP-1 to regulate meiotic progression. Biochemical analysis demonstrates that these mutations
156 limit the ability of meiotic HORMADs to adopt their closed conformations. Taken together, our
157 work shows that PCH-2's remodeling of meiotic HORMADs from closed to unlocked
158 conformations decelerates pairing, synapsis, recombination, and meiotic progression, to
159 proofread homolog interactions and maintain meiotic fidelity. Further, PCH-2 cleanly delegates
160 its regulation of different meiotic prophase events to different meiotic HORMADs, offering new
161 insight into how PCH-2 mechanistically coordinates the events of pairing, synapsis, and
162 recombination. Lastly, it provides a potential explanation for why this family of meiotic
163 HORMADs has dramatically expanded in *C. elegans* and what this suggests about the
164 evolutionary role of HORMADs during meiosis.
165

166 **Results**

167 PCH-2's localization is consistent with remodeling HORMADs on the axial elements of meiotic
168 chromosomes

169 Meiotic HORMADs collaborate with cohesins and other axial proteins to organize meiotic
170 chromosomes into linear axial elements functionally capable of undergoing interhomolog
171 pairing, synapsis and recombination (Ur & Corbett, 2021). While PCH-2 has been implicated in
172 remodeling meiotic HORMADs away from meiotic chromosomes to ensure their availability
173 (Herruzo et al., 2021; Herruzo et al., 2016) and entry into the nucleus (Yang, Hu, Portheine,
174 Chuenban, & Schnittger, 2020), its localization to meiotic chromosomes before and after
175 synapsis (Cuacos et al., 2021; Deshong et al., 2014; Joshi et al., 2009; Lambing et al., 2015;
176 San-Segundo & Roeder, 1999) suggests a role remodeling meiotic HORMADs on
177 chromosomes as well. To test this, we used structured illumination microscopy to more closely

178 investigate whether PCH-2's localization was consistent with remodeling meiotic HORMADs on
179 axial elements.

180 Before synapsis and during axis assembly, PCH-2 localizes to foci on meiotic chromosomes.
181 After synapsis, PCH-2 localizes along the synaptonemal complex and this localization is
182 dependent on the central element component SYP-1 (Deshong et al., 2014), which assembles
183 between axial elements during synapsis (Figure 1A). We performed indirect
184 immunofluorescence on wildtype meiotic nuclei against both PCH-2 and SYP-1 and performed
185 structured illumination microscopy to resolve the distance between axial elements (Figure 1B)
186 (Carlton, 2008). While SYP-1 appeared as a line of continuous width in all meiotic nuclei, PCH-2
187 staining often appeared wider than SYP-1, often splitting as parallel tracks with SYP-1 staining
188 between PCH-2 tracks (arrows), indicating that PCH-2 can reside on or close to axial elements
189 of synapsed chromosomes and remodel meiotic HORMADs on chromosomes.

190 *htp-3* ^{H96Y} suppresses the acceleration of pairing and synapsis in *pch-2* mutants

191 Having established that PCH-2's localization is consistent with the ability to remodel meiotic
192 HORMADs on meiotic chromosomes, we looked for genetic interactions that might support this
193 possibility. *htp-3(vc75)* is a missense mutation that replaces histidine 96 with a tyrosine in the
194 HORMA domain (H96Y) (Figure 2A). HTP-3^{H96Y} properly localizes to meiotic chromosomes
195 (Couteau & Zetka, 2011) and does not affect pairing, synapsis and crossover recombination
196 (Bohr, Nelson, Giacopazzi, Lamelza, & Bhalla, 2018; Couteau & Zetka, 2011). However, we and
197 others previously showed that this mutation in *htp-3* abolished meiotic checkpoint responses in
198 *C. elegans* (Bohr et al., 2018; Couteau & Zetka, 2011). Because of this phenotype, we analyzed
199 HTP-3's relationship with PCH-2 in regulating pairing, synapsis, recombination, and meiotic
200 progression.
201

202 To test whether PCH-2 genetically interacts with HTP-3 to regulate pairing, we generated *pch-*
203 *2;syp-1* double mutants, *htp-3^{H96Y};syp-1* double mutants, and *pch-2;htp-3^{H96Y};syp-1* triple
204 mutants and assessed pairing when compared with *syp-1* single mutants. SYP-1 is a central
205 element protein of the synaptonemal complex (SC) (MacQueen, Colaiacovo, McDonald, &
206 Villeneuve, 2002). *syp*-1 null mutants successfully undergo pairing despite the failure to load SC
207 components, particularly at specific loci called Pairing Centers (PCs) (MacQueen et al., 2002).
208 Therefore, these experiments allow us to analyze pairing independent of synapsis. We
209 performed immunofluorescence against the HIM-8 protein, which localizes to PCs on the X
210 chromosome (Phillips et al., 2005), to assess pairing at this locus throughout the germline: two
211 HIM-8 foci indicate the X-chromosomes are unpaired while a single HIM-8 focus indicates
212 paired X-chromosomes. Because meiotic nuclei are arranged in spatiotemporal gradient in
213 germlines, we divided the germline into six equivalently sized zones to perform a meiotic time-
214 course and determined the percentage of nuclei with a single HIM-8 focus in each zone (Figure
215 3A and 3B).
216
217 Similar to previous work (Deshong et al., 2014; Giacopazzi et al., 2020), we found that there is
218 an increase in percentage of nuclei with paired X chromosomes in zone 2 for *pch-2;syp-1*
219 double mutants (76%, Figure 3C) compared to *syp-1* single mutant controls (49%, Figure 3C),
220 showing that the rate of pairing is accelerated in the absence of *pch-2. htp-3^{H96Y};syp-1* double
221 mutants have a similar rate of pairing compared to *syp-1* single mutant controls (46%, Figure
222 3C), demonstrating that this mutation does not affect the rate of pairing. Interestingly, we found
223 that *pch-2;htp-3^{H96Y};syp-1* triple mutants have a similar rate of pairing compared to *syp-1* single
224 mutants and *htp-3^{H96Y};syp-1* double mutants (49%, Figure 3C), indicating that *htp-3^{H96Y}*
225 suppresses the acceleration of pairing observed in *pch-2* mutants.
226

227 Next, we tested for a genetic interaction between *pch-2* and *htp-3* during synapsis. We analyzed
228 the rate of synapsis in germlines from control, *pch-2* single mutants, *htp-3*^{H96Y} single mutants,
229 and *pch-2;htp-3*^{H96Y} double mutant worms by performing immunofluorescence against the axial
230 element HTP-3 (Goodyer et al., 2008; MacQueen et al., 2005) and the central element SYP-1
231 (MacQueen et al., 2002). We then determined the fraction of nuclei with complete synapsis in
232 each zone. Complete synapsis is visible as full co-localization of HTP-3 and SYP-1, whereas
233 nuclei with incomplete synapsis have stretches of HTP-3 without SYP-1 signal (arrowheads,
234 Figure 3D). Similar to previous data, we report that *pch-2* null mutants have an accelerated rate
235 of synapsis (61%, Figure 3E) compared to wildtype controls (33%, Figure 3E) in zone 2 and a
236 delay in desynapsis in zone 6 (Deshong et al., 2014; Giacopazzi et al., 2020) (Figure 3E). *htp-*
237 *3*^{H96Y} single mutants have a similar rate of synapsis compared to wildtype controls (36%, Figure
238 3E), suggesting that the rate of synapsis is unaffected in this background, and accelerated
239 desynapsis, as previously reported (Couteau & Zetka, 2011). Analogous to our pairing results,
240 we found that *pch-2;htp-3*^{H96Y} double mutants have a similar rate of synapsis compared to
241 wildtype controls and *htp-3*^{H96Y} single mutants (34%, Figure 3E), indicating that *htp-3*^{H96Y}
242 suppresses the acceleration of synapsis in *pch-2* mutants.
243
244 To further solidify that PCH-2 acts on HTP-3 to regulate synapsis, we analyzed synapsis in
245 *meDf2* heterozygotes (*meDf2/*+). *meDf2* is a mutation in which PC regions are deleted from the
246 X chromosome (Villeneuve, 1994). Since PCs are essential for pairing and synapsis
247 (MacQueen et al., 2005), *meDf2* homozygotes fail to pair and synapse X chromosomes while
248 *meDf2* heterozygotes behave like a partial loss of function mutation: ~50% of nuclei complete
249 synapsis of X chromosomes while the remaining 50% have unsynapsed X chromosomes
250 (MacQueen et al., 2005). In *pch-2;meDf2*/+ worms, ~85% of nuclei complete synapsis,
251 demonstrating that PCH-2 normally inhibits synapsis when PC function is compromised
252 (Deshong et al., 2014).

253

254 To test whether *htp-3*^{H96Y} also suppressed the synapsis in *pch-2;meDf2*/+ worms, we generated
255 *pch-2;htp-3*^{H96Y}*;meDf2*/+ triple mutants and analyzed the rate of synapsis, comparing it to
256 controls. Similar to previous results, we found that 87% of nuclei in *pch-2;meDf2/*+ double
257 mutants achieve complete synapsis in zone 5 compared to 48% complete synapsis for *meDf2/*+
258 single mutant worms (Figure 3F). *htp-3*^{H96Y}*;meDf2/*+ worms have 52% of nuclei with complete
259 synapsis in zone 5, similar to *meDf2/*+ single mutants (Figure 3F). *pch-2;htp-3*^{H96Y}*;meDf2*/+
260 triple mutants show maximal levels of synapsis in zone 4 (36%, Figure 3F) and more closely
261 resemble the levels of synapsis observed in to *htp-3*^{H96Y}*;meDf2/*+ double and *meDf2/*+ single
262 mutants than *pch-2;meDf2/*+ double mutants. These data indicate that PCH-2's ability to inhibit
263 synapsis when PC function is compromised depends on the function of the HORMA domain of
264 HTP-3, similar to what we observed when PCs are fully functional (Figure 3E). To determine
265 whether these defects in synapsis produce chromosome segregation errors, we scored the
266 percent of male progeny in these strains. Male progeny, which are genotypically XO in contrast
267 to XX hermaphrodites, are diagnostic of misegregation of X chromosomes in meiosis. The
268 ability of *htp-3*^{H96Y} to suppress the synapsis of X chromosomes in *pch-2;meDf2/*+ was further
269 supported by the increase in male progeny observed in *pch-2;htp-3* ^{H96Y}*;meDf2/*+ triple mutants
270 (10.84%, Table 1) in comparison to *pch-2;meDf2/*+ double mutants (0.83%, Table 1).

271 <u>*htp-3* ^{H96Y} exacerbates defects in DNA repair and crossover formation in *pch-2* mutants</u>

272 We next tested whether PCH-2 regulates recombination through HTP-3 by assaying DNA repair
273 and crossover formation in *pch-2;htp-3*^{H96Y} double mutants. The rate of DNA repair is assessed
274 by quantifying the number of RAD-51 foci per nucleus throughout the germline (Figure 3G). The
275 appearance of RAD-51 foci on meiotic chromosomes is associated with the introduction of
276 double-strand breaks and their disappearance is associated with the entry of double-strand
277 breaks into repair pathways (Colaiacovo et al., 2003). RAD-51 numbers peak in zone 4 in

278 wildtype animals, increasing to an average of 2 per nuclei, and decrease as RAD-51 is removed
279 during DNA repair. *pch-2* single mutants have a lower average of RAD-51 foci per nucleus in
280 zones 4-6 (Figure 3H), consistent with previous findings that that *pch-2* mutants exhibit a faster
281 rate of DNA repair compared to wildtype controls (Deshong et al., 2014). *htp-3*^{H96Y} single
282 mutants show a similar rate of DNA repair as wildtype germlines (Figure 3H), although the
283 average number of RAD-51 foci is slightly lower than wildtype (Couteau & Zetka, 2011). By
284 contrast, *pch-2;htp-3*^{H96Y} double mutants not only show an accelerated rate of DNA repair,
285 similar to *pch-2* single mutants, they have a reduced average number of RAD-51 foci in zone 5
286 (0.75 foci, Figure 3H), showing that mutation of *htp-3* exacerbates the acceleration of DNA
287 repair in *pch-2* mutants. Because *htp-3*^{H96Y} and *pch-2* mutants do not have reduced numbers of
288 double-stranded breaks (Couteau & Zetka, 2011; Deshong et al., 2014), these results reflect
289 changes in the rate of DNA repair. Further, this indicates that, in contrast to our findings for
290 pairing and synapsis, PCH-2 does not act through HTP-3 to regulate the rate of DNA repair.
291 Instead, both proteins regulate DNA repair independent of each other.
292
293 We previously reported that *pch-2;htp-3*^{H96Y} double mutants exhibit more achiasmate
294 chromosomes than either single mutant (Deshong et al., 2014), indicating that the double
295 mutant has a more severe defect in meiotic crossover recombination than either single mutant
296 and consistent with our analysis of DNA repair (Figure 3H). To further verify this result on
297 crossover formation, we quantified the number of GFP::COSA-1 foci for each meiotic nucleus.
298 COSA-1 is a cyclin-like protein that localizes specifically to presumptive crossovers, serving as
299 a cytological marker for crossover formation (Yokoo et al., 2012). Because *C. elegans* contain 6
300 pairs of chromosomes and exhibit strong crossover interference, most wildtype nuclei have 6
301 GFP::COSA-1 foci per nucleus (Figure 3I) (Yokoo et al., 2012). Our findings also reflect this,
302 where we report only 3% of nuclei have less than 6 GFP::COSA-1 foci (Figure 3J). We also
303 found that the incidence of nuclei with less than 6 GFP::COSA-1 foci increases to 9% of nuclei

304 in *pch-2* single mutants (Figure 3J), recapitulating previous findings that *pch-2* mutants exhibit a
305 loss of crossover assurance (Deshong et al., 2014; Giacopazzi et al., 2020). *htp-3*^{H96Y} single
306 mutants also show an increase in the number of nuclei with less than 6 GFP::COSA-1
307 crossovers compared to wildtype (7%, Figure 3J), consistent with their checkpoint role (Couteau
308 & Zetka, 2011). Similar to our analysis of DNA repair, the number of nuclei with less than 6
309 GFP::COSA-1 foci in *pch-2;htp-3*^{H96Y} double mutants increases to 11% percent (Figure 3J),
310 showing an additive effect for crossover defects. These data illustrate that PCH-2 and HTP-3
311 work independently to regulate crossover formation.
312
313 Altogether, our analysis of pairing, synapsis and crossover recombination indicate that PCH-2
314 and HTP-3 act together to regulate pairing and synapsis but independently to regulate DNA
315 repair and crossover formation. More specifically, these data strongly support a model in which
316 PCH-2 acts through HTP-3's HORMA domain to control the rate of pairing and synapsis but not
317 the process of meiotic recombination.

318 <u>*htp-3*^{H96Y} does not affect meiotic progression</u>

319 In budding yeast, Pch2's remodeling of the meiotic HORMAD, Hop1, contributes to meiotic
320 progression (Raina & Vader, 2020a). Since *htp-3*^{H96Y} mutants genetically interact with *pch-2*
321 mutants in *C. elegans*, we also tested whether *htp-3*^{H96Y} mutants affected meiotic progression.
322 We assessed meiotic progression by performing immunofluorescence against a factor required
323 for double-strand break formation, DSB-1 (Figure S1A). DSB-1 localizes to meiotic
324 chromosomes to facilitate double-strand break formation (Stamper et al., 2013). In response to
325 meiotic defects, DSB-1 persists on chromosomes to maintain a period of competency for
326 double-strand break formation to promote crossover assurance (Stamper et al., 2013). We
327 quantified the fraction of meiotic nuclei that were positive for DSB-1 and could not detect any

328 difference between control and *htp-3*^{H96Y} mutant germlines (Figure S1B), illustrating that this
329 mutation does not affect meiotic progression.
330
331 A null mutation in *htp-3* abolishes the delay in meiotic progression observed when there are
332 defects in synapsis, such as in *syp-1* mutants (Kim et al., 2015). To determine whether *htp-3*^{H96Y}
333 affected meiotic progression in *syp-1* mutants, we quantified the fraction of DSB-1 positive
334 meiotic nuclei in both *syp-1* single mutants and *syp-1;htp-3*^{H96Y} double mutants and could not
335 observe any difference between these genotypes (Figure S1C), indicating that *htp-3*^{H96Y} does
336 not affect the extension of meiotic progression observed when there are meiotic defects.

337 <u>*him-3*^{R93Y} does not suppress the acceleration of pairing or synapsis in *pch-2* mutants</u>

338 Our findings that PCH-2 acts on HTP-3 to promote pairing and synapsis, but not recombination,
339 indicates that PCH-2 regulates recombination through an HTP-3 independent mechanism.
340 Further, it is unclear whether PCH-2 regulates pairing and synapsis only through its interaction
341 with HTP-3 or whether other meiotic HORMADs also contribute to this regulation. To address
342 these possibilities, we next tested whether *pch-2* genetically interacts with similar mutations in
343 *him-3* or *htp-1*, genes that encode the two other HORMADs essential for meiosis in *C. elegans*.
344
345 We performed a Clustal Omega alignment of HTP-3 with the other three meiotic HORMADs
346 (Sievers et al., 2011) and observed that the mutation in *htp-3*^{H96Y} was not of a conserved
347 residue but was adjacent to two invariant residues in all four meiotic HORMADs (red box in
348 Figure 2B). Further, based on this alignment, the arginine at position 93 of HIM-3 should be
349 positioned similarly within the HORMA domain (Figures 2C and D). Using CRISPR/Cas9 gene
350 editing, we made a corresponding missense mutation to the *htp-3*^{H96Y} allele in *him*-3, where
351 arginine 93 was replaced with a tyrosine (*him-3*^{R93Y}). Indirect immunofluorescence verified that

352 this mutation did not affect HIM-3's localization to chromosomes (Figure S2), progeny viability or
353 the production of male progeny (Table 1).
354
355 First we analyzed pairing in *syp-1*, *pch-2;syp-1*, *him-3^{R93Y};syp-1*, and *pch-2;him-3^{R93Y};syp-1*
356 mutants by performing immunofluorescence against HIM-8 (Figure 4A and 4B). *him-3^{R93Y};syp-1*
357 double mutants show 44% of nuclei completed pairing in zone 2, similar to *syp-1* single mutants,
358 demonstrating that this mutation does not affect pairing (Figure 4B). In contrast to our analysis
359 of the *htp-3^{H96Y}* allele, we found that *pch-2;him-3^{R93Y};syp-1* triple mutants also show an
360 accelerated rate of pairing phenotype (63%, Figure 4B) similar to that of *pch-2;syp-1* double
361 mutants. Therefore, we detect no genetic interaction between *pch-2* and *him-3^{R93Y}* in affecting
362 the rate of pairing.
363
364 Next, we assessed the rate of synapsis in wildtype, *pch-2*, *him-3^{R93Y}*, and *pch-2;him-3^{R93Y}*
365 germlines by performing immunofluorescence against SYP-1 and HTP-3 (Figure 4C and 4D). In
366 both *pch-2* and *him-3^{R93Y}* single mutants, we found that there was an increase in the number of
367 nuclei that completed synapsis in zone 2 (13% for both, compared to the wildtype control of 3%,
368 Figure 4D), suggesting that synapsis is accelerated in both mutants. However, we found that
369 *pch-2;him-3^{R93Y}* double mutants display more severe synapsis defects than either single mutant:
370 the rate of synapsis is delayed throughout zones 2-5 and these double mutants reach only 87%
371 complete synapsis throughout the germline (Figure 4D). These results demonstrate that PCH-2
372 and HIM-3 regulate the progression of synapsis independent of each other.
373
374 Finally, we further assessed synapsis in *him-3^{R93Y} and pch-2;him-3^{R93Y}* mutants by scoring
375 synapsis in *meDf2* heterozygotes (*meDf2/*+). Consistent with a role in regulating synapsis, *him-*
376 *3^{R93Y};meDf2/*+ double mutants show a reduced rate of synapsis (Figure 4E) compared to
377 *meDf2/*+ controls (see zones 4 and 5). This effect was intermediate in *pch-2;him-3^{R93Y}*;*meDf2/*+

378 triple mutant worms, providing further support that PCH-2 and HIM-3 both regulate synapsis but
379 accomplish this through independent mechanisms.

380 *him-3^{R93Y}* does not suppress DNA repair defects in *pch-2* mutants

381 We next tested whether *pch-2* genetically interacts with *him-3^{R93Y}* during the regulation of DNA
382 repair by scoring RAD-51 foci in N2, *pch-2*, *him-3^{R93Y}* and *pch-2;him-3^{R93Y}* mutants (Figure 4F).
383 In *him-3^{R93Y}* single mutants, the average number of RAD-51 foci was higher in zone 3 than both
384 *pch-2* and control germlines, suggesting a more rapid installation of RAD-51 and potentially
385 more double strand breaks. However, the rate of DNA repair was similar to wildtype (Figure
386 4G). *pch-2*;*him-3^{R93Y}* worms more closely resembled *him-3^{R93Y}* single mutants than *pch-2* single
387 mutants in zone 3 but was intermediate between *him-3^{R93Y}* and *pch-2* single mutants in zone 4
388 (Figure 4G), indicating that the accelerated rate of DNA repair observed in *pch-2* mutants is not
389 fully suppressed by the *him-3^{R93Y}* mutation and that these two factors do not act in the same
390 pathway to regulate DNA repair.

391 *him-3^{R93Y}* suppresses crossover recombination defects in *pch-2* mutants

392 To analyze the effect of *him-3^{R93Y}* on crossover recombination, and test for a genetic interaction
393 with *pch-2* mutants, we scored GFP::COSA-1 foci in wildtype, *pch-2, him-3^{R93Y}* and *pch-2;him-*
394 *3^{R93Y}* mutant strains (Figure 4H). Similar to *pch-2* single mutants, we found that there was an
395 increase of nuclei with less than 6 GFP::COSA-1 foci in *him-3^{R93Y}* mutants compared to wildtype
396 controls (9%, Figure 4I), showing that mutation of this residue in HIM-3 causes a loss of
397 crossover assurance. In contrast to *pch-2;htp-3^{H96Y}* double mutants (Figure 3J), *pch-2;him-3^{R93Y}*
398 double mutants have a reduced number of nuclei with less than 6 foci compared to either single
399 mutant and more closely resembles the frequency observed in wildtype nuclei (5%, Figure 4I).
400 Therefore, *him-3^{R93Y}* suppresses the defect on crossover assurance observed in *pch-2* mutants.

401

402 We next visualized whether we could observe this genetic suppression later in meiotic
403 prophase, when chromosome pairs are linked by chiasmata. Wildtype *C. elegans* oocytes
404 contain 6 pairs of chromosomes or bivalents, and these can be visualized as 6 “DAPI stained
405 bodies”. Defects in recombination produce homologs without chiasmata, or univalents, in
406 oocytes (arrows, Figure 4J). In our analysis of wildtype oocytes, we did not observe any
407 univalents (Figure 4K). Similar to our previous findings (Deshong et al., 2014), we found that
408 there was an increase in the percent of nuclei with univalents in *pch-2* single mutants compared
409 to wildtype controls (0.8%, Figure 4K), further demonstrating a loss of crossover assurance that
410 leads to achiasmate homolog pairs. Correlating with our GFP::COSA-1 analysis, *him-3*^{R93Y}
411 single mutants also have an increase in the number of oocytes containing univalents (1.3%,
412 Figure 4K), demonstrating that *him-3*^{R93Y} mutants also observe a loss of crossover assurance.
413 In *pch-2;him-3*^{R93Y} double mutants, we found no instances of univalents (Figure 4K), further
414 indicating that these two mutant alleles genetically suppress each other in the context of
415 crossover recombination.
416

417 Taken together, our results are consistent with a model in which PCH-2 acts through HIM-3 to
418 promote crossover recombination but not pairing or synapsis. Further, the roles of the two
419 meiotic HORMADs appear to be cleanly delegated, with PCH-2 controlling pairing and synapsis
420 through HTP-3 and crossover recombination through HIM-3. Since we do not observe a similar
421 genetic interaction when we analyze DNA repair in *pch-2;him-3*^{R93Y} double mutants, this
422 regulation of crossover recombination occurs later than the installation and removal of RAD-51.

423 <u>*him-3*^{R93Y} does not affect meiotic progression</u>

424 We next tested whether *him-3*^{R93Y} mutants affect meiotic progression by performing
425 immunofluorescence against DSB-1 and quantifying the fraction that were DSB-1 positive in

426 wildtype and *him-3*^{R93Y}mutant strains (Figure S3A). We found that there was not a significant
427 difference between the number of DSB-1 positive nuclei between wildtype and *him-3*^{R93Y} mutant
428 strains (Figure S3B), suggesting that this mutation does not affect meiotic progression.
429
430 We further tested whether the *him-3*^{R93Y} mutation affected meiotic progression by quantifying
431 the fraction of DSB-1 positive nuclei in *syp-1* and *him-3*^{R93Y}*;syp-1* mutant strains. Similar to our
432 findings for *htp-3*^{H96Y}*,* we found that there was not a significant difference in the number of DSB-
433 1 positive nuclei between *syp-1* single mutant*s* and *him-3*^{R93Y}*;syp-1* double mutants (Figure
434 S3C). This result further demonstrates that *him-3*^{R93Y} does not affect meiotic progression.
435
436 <u>*htp-1*^{G97T} does not suppress the accelerated rate of pairing in *pch-2* mutants</u>
437
438 Our findings suggest that PCH-2 acts through HTP-3 to promote pairing and synapsis, and HIM-
439 3 to promote crossover formation. We next wanted to test whether *pch-2* genetically interacts
440 with a similar mutation in *htp-1*, the gene that encodes the final essential meiotic HORMAD in *C.*
441 *elegans*.

442 Preliminary structural analysis of the HORMA domain of HTP-1 indicates that the glycine
443 residue that is analogous to the histidine and arginine residues of HTP-3 and HIM-3 (Figure 2B),
444 respectively, is positioned more internally within the HORMA domain (Figure 2E) and therefore
445 potentially more constrained in the mutations we can introduce at this site without affecting
446 HTP-1's stability. Indeed, when we replaced this glycine with a tyrosine by CRISPR/Cas9 gene
447 editing (*htp-1*^{G97Y}*)*, this mutant phenotypically resembled the *htp-1*(*me84)* null allele (Martinez-
448 Perez & Villeneuve, 2005) in which this glycine residue is mutated to a glutamate, producing
449 very few viable progeny and a high incidence of male (HIM) phenotype. Given that the severity
450 of the *htp-1*^{G97Y} mutation would preclude our analysis of meiotic prophase events, we sought to

451 create a less severe hypomorphic allele of HTP-1 to test whether it genetically interacts with the
452 *pch-2* null mutation.

453 To identify a mutation that would allow analysis of pairing, synapsis, recombination, and meiotic
454 progression, we used CRISPR/Cas9 to substitute glycine 97 with amino acids that progressively
455 add bulkier side chains at this position (*htp-1*^{G97A}, *htp-1*^{G97S}*, and htp-1*^{G97T}). Upon initial
456 examination of these strains, we observed a HIM phenotype associated with the *htp-1*^{G97T}
457 mutant strain (Table 1), suggesting that this mutation causes meiotic chromosome
458 misegregation. This HIM phenotype was accompanied by a reduction in embryonic viability
459 (Table 1). Therefore, we limited our analysis of testing genetic interactions with *pch-2* for
460 pairing, synapsis, and recombination to *htp-1*^{G97T} mutants. Indirect immunofluorescence showed
461 no difference in the loading of HTP-1 to meiotic chromosomes in *htp-1*^{G97T} mutants (Figure S4).
462
463 We first tested whether pairing is disrupted in this strain by performing immunofluorescence
464 against HIM-8 in *syp-1*, *pch-2;syp-1*, *htp-1*^{G97T};*syp-1* and *pch-2*;*htp-1*^{G97T};*syp-1* mutant germlines
465 (Figure 5A and 5B). In *htp-1*^{G97T};*syp-1* double mutants, the percent of nuclei that have
466 completed pairing in zone 2 is similar compared to *syp-1* single mutants (Figure 5B), indicating
467 that *htp-1*^{G97T};*syp-1* double mutants do not have a defect in the progression of pairing. *pch-*
468 *2;htp-1*^{G97T};*syp-1* triple mutants have a similar rate of pairing in zone 2 compared to *pch-2;syp-1*
469 double mutants (Figure 5B), showing that the *htp-1*^{G97T} mutation does not suppress the
470 acceleration of pairing observed in *pch-2* mutants.
471
472 <u>*htp-1*^{G97T} causes severe synapsis defects that are not suppressed by mutation of *pch-2*</u>
473
474 Next, we tested whether synapsis is perturbed in *htp-1*^{G97T} mutants and whether this allele
475 genetically interacts with the *pch-2* null allele (Figure 5C and 5D). Synapsis is severely

476 disrupted in *htp-1*^{G97T} mutants: despite some chromosomes completing synapsis (Figure 5D),
477 almost all meiotic nuclei have some number of unsynapsed chromosomes throughout the
478 germline, where only 1.3% of nuclei reach complete synapsis (Figure 5D). In *pch-2*;*htp-1*^{G97T}
479 double mutants, we find that synapsis is disrupted as severely as *htp-1*^{G97T} single mutants,
480 where 1.3% of nuclei also reach complete synapsis (Figure 5D), indicating that these alleles do
481 not genetically interact and regulate synapsis independent of each other.
482
483 <u>*htp-1*^{G97T} leads to a delay in RAD-51 removal that is not suppressed by mutation of *pch-2*</u>
484
485 Next, we assessed the progress of DNA repair in *htp-1*^{G97T} and *pch-2*;*htp-1*^{G97T} mutants by
486 scoring RAD-51 foci throughout the germline (Figure 5E and 5F). In comparison to control
487 germlines, *htp-1*^{G97T} single mutants exhibit a delay in the installation of RAD-51 foci (Figure 5F).
488 However, as meiotic prophase continues, meiotic nuclei in *htp-1*^{G97T} single mutants have more
489 RAD-51 foci and substantially delay their removal, possibly as an indirect consequence of the
490 defects in synapsis we observe in this mutant (Figure 5D). *pch-2*;*htp-1*^{G97T} double mutants no
491 longer exhibit this delay in RAD-51 installation, suggesting a partial suppression of this
492 particular phenotype, but display more RAD-51 foci, particularly in zones 4 and 5, than wildtype
493 meiotic nuclei and *pch-2* single mutants, similar to *htp-1*^{G97T} single mutants. Thus, PCH-2 and
494 HTP-1 do not appear to genetically interact to regulate the rate of DNA repair.
495
496 <u>*htp-1*^{G97T} causes defects in crossover recombination that are not suppressed by *pch-2*
497 mutations</u>
498
499 To continue our analysis, we analyzed crossover recombination by scoring the number of
500 GFP::COSA-1 foci per nucleus in wildtype, *pch-2*, *htp-1*^{G97T}, and *pch-2*;*htp-1*^{G97T} mutants
501 (Figure 5G and 5H). Surprisingly, we found that in *htp-1*^{G97T} single mutants, the number of

502 COSA-1 foci varies greatly across nuclei, ranging from 4 to 9, with only 39% of nuclei have 6
503 GFP::COSA-1 foci (Figure 5H), suggesting that the *htp-1*^{G97T} mutation causes misregulation of
504 crossover formation. We attribute this loss of crossover assurance to the synapsis defects we
505 observe in *htp-1*^{G97T} mutants (Figure 5D). In *pch-2*;*htp-1*^{G97T} double mutants, we observe a
506 similar phenotype where the number of GFP::COSA-1 varies across nuclei, ranging from 4 to 9,
507 with only 45% having 6 COSA-1 foci (Figure 5H). Overall, these data indicate that PCH-2 and
508 HTP-1 do not genetically interact to regulate crossover recombination.
509
510 We further analyzed crossover formation by looking directly at bivalents in oocytes and
511 quantified the frequency of univalents in wildtype, *pch-2*, *htp-1*^{G97T}, and *pch-2*;*htp-1*^{G97T} mutants
512 (Figure 5I and 5J). In *htp-1*^{G97T} single mutants, we found that the frequency of univalents
513 significantly increases to 41% (Figure 5J), further verifying the defect in crossover formation in
514 *htp-1*^{G97T} single mutants. For *pch-2*;*htp-1*^{G97T} double mutants, we also found that the frequency
515 of univalents is statistically higher compared to wildtype oocytes but not significantly different
516 when compared to *htp-1*^{G97T} single mutants (31%, Figure 5J). Taken together, this suggests that
517 both *pch-2* and *htp-1* both promote crossover assurance but regulate it through different
518 mechanisms.
519
520 <u>*htp-1*^{G97T} delays meiotic progression and this delay is partially suppressed by mutation of *pch-2*</u>
521
522 The absence of HTP-1 accelerates meiotic progression, producing non-homologous synapsis
523 and more rapid DNA repair (Martinez-Perez & Villeneuve, 2005). In contrast, mutations within
524 the HORMA domain of HTP-1 that prevent its loading on meiotic chromosomes cause a delay in
525 meiotic progression, producing asynapsis (Silva et al., 2014). We tested whether *htp-1*^{G97T}
526 mutations similarly affect meiotic progression by performing immunostaining against DSB-1.
527

528 We quantified the fraction of DSB-1 positive meiotic nuclei in wildtype and *htp-1*^{G97T} mutant
529 germlines (Figure 6A). We found that *htp-1*^{G97T} mutants display a statistically significant increase
530 in the fraction of DSB-1 positive nuclei (81%, Figure 6B), suggesting that this mutation produces
531 a delay in meiotic progression. Since DSB-1 is required for double strand break formation, the
532 extension of DSB-1 likely explains the increase in RAD-51 foci (Figure 5F) and the loss of
533 crossover interference (Figure 5H) in *htp-1*^{G97T} mutants. Given the severity of this phenotype,
534 we wondered if the less severe mutations we generated, *htp-1*^{G97A} and *htp-1*^{G97S} mutants, might
535 also affect meiotic progression, albeit more weakly (Figure 6A). While *htp-1*^{G97A} mutants did not
536 affect the fraction of DSB-1 positive nuclei, *htp-1*^{G97S} mutants produced a small but statistically
537 significant delay in meiotic progression (63% DSB-1 positive nuclei, Figure 6B), indicating that
538 the introduction of bulkier amino acids at this residue produces an allelic series with respect to
539 defects in meiotic progression.
540
541 We next tested whether this defect in meiotic progression in *htp-1*^{G97T} single mutants is
542 suppressed by the *pch-2* mutation. We found that the percent of DSB-1stained nuclei is slightly
543 but significantly lower in *pch-2*;*htp-1*^{G97T} double mutants (77%, Figure 6B) compared to *htp-1*^{G97T}
544 single mutants (Figure 6B), indicating that the meiotic progression defect in *htp-1*^{G97T} mutants is
545 partially suppressed by mutations in *pch-2* and that these two proteins cooperate to regulate
546 meiotic progression.
547
548 <u>*him-3*^{R93Y} mutants maintain the structure of the HORMA domain but have reduced affinity for</u>
549 <u>closure motifs</u>
550
551 Our data thus far demonstrates that *pch-2* genetically interacts with specific alleles of *htp-3*,
552 *him-3* and *htp-1*, with varying effects on pairing, synapsis, recombination and meiotic
553 progression. However, how these genetic interactions translate into a molecular understanding

554 of the functional relationship between PCH-2 and these meiotic HORMADs is unclear. To
555 address this, we tested what effect these mutations had on the ability of meiotic HORMADs to
556 bind their closure motifs and adopt the closed conformation.
557
558 While the closure motif for HTP-3 is unknown, HIM-3 is known to bind closure motifs found
559 within the C-terminal tail of HTP-3 (Kim et al., 2014b). We cloned and expressed wildtype HIM-3
560 and HIM-3^{R93Y} in *E. coli*, purified each protein, and performed a fluorescence polarization
561 peptide binding assay to test how well HIM-3^{R93Y} binds this closure motif peptide *in vitro*. We
562 found that wildtype HIM-3 binds its closure motif with a K_d of 220 +/- 20 nM and found that it
563 does not bind to scramble motif controls (Figure 7A). However, HIM-3^{R93Y} binds to the same
564 closure motif with an increased K_d of 690 +/- 130 nM, indicating that HIM-3^{R93Y} binds its closure
565 motif with reduced affinity compared to wildtype HIM-3 (Figure 7A). Additionally, we found the
566 stability of these two proteins to be similar (Figure S5) and the structure of the HIM-3^{R93Y}
567 HORMA domain to be similar to that of wildtype HIM-3 (Figure 2D), suggesting that reduced
568 affinity for the closure motif for HIM-3^{R93Y} is not due to instability of the protein or an inability to
569 adopt the closed conformation. These results demonstrate that HIM-3^{R93Y} cannot bind its
570 closure motif as readily as wildtype HIM-3, limiting its ability to adopt the closed conformation *in*
571 *vivo* (Figure 7B). Because this residue is positioned similarly within all three-essential meiotic
572 HORMADs (Figure 2B), our biochemical analysis of HIM-3^{R93Y} may be generalizable to the
573 mutant versions of HTP-3 and HTP-1: HTP-3^{H96Y} and HTP-1^{G97T} likely bind their respective
574 closure motifs with less affinity and preferentially reside in an unlocked or unbuckled
575 conformation *in vivo*.
576
577 When combined with the localization of PCH-2 by structured illumination microscopy (Figure 1)
578 and our genetic and cytological analysis (Figures 3-6) of how these mutant alleles suppress
579 some defects observed in *pch-2* mutants, these data are entirely consistent with PCH-2

580 remodeling meiotic HORMADs from a closed to unlocked conformation on meiotic
581 chromosomes to control the progress of pairing, synapsis, meiotic recombination and cell cycle
582 progression.
583
584 **Discussion**
585 Since the identification of Pch2 in budding yeast more than 20 years ago (San-Segundo &
586 Roeder, 1999), the particular role of PCH-2 during meiosis has been enigmatic. More recently,
587 biochemical and structural analysis of PCH-2's ability to remodel HORMADs (Alfieri et al., 2018;
588 Clairmont et al., 2020; Ye et al., 2017; Ye et al., 2015) has provided a useful framework to
589 imagine PCH-2's role in meiosis, particularly given the essential role closed conformations of
590 meiotic HORMADs play in structuring chromosomes for homolog pairing, synapsis and
591 recombination and signaling meiotic progression (Kim et al., 2014b). However, despite this
592 framework, important questions remain unanswered: Since PCH-2 is present on meiotic
593 chromosomes prior to synapsis and not all systems remove meiotic HORMADs in response to
594 synapsis: 1) Are there biological consequences for remodeling meiotic HORMADs aside from
595 regulating meiotic progression and shuttling meiotic HORMADs into the nucleus? 2) Are
596 unbuckled or unlocked versions of meiotic HORMADs functionally inert, similar to open Mad2,
597 or do they have some biological relevance *in vivo*? 3) In systems with multiple meiotic
598 HORMADs, do these meiotic HORMADs carry out different functions, at least in the context of
599 regulation by PCH-2?
600
601 Our experiments from this study in *C. elegans* answer many of these questions. We previously
602 showed that a null mutation of *pch-2* accelerates the rates of pairing, synapsis and meiotic
603 recombination, leading to a loss of meiotic fidelity (Deshong et al., 2014). Our identification of
604 mutations in the HORMA domains of both HTP-3 and HIM-3 (Figure 2A) that suppress these
605 defects is consistent with a model in which PCH-2 controls the rate of pairing, synapsis and

606 meiotic recombination through an interaction with these domains in HTP-3 and HIM-3 on meiotic
607 chromosomes. For HTP-3, this regulation likely happens prior to synapsis when PCH-2 is
608 present as foci on meiotic chromosomes. For HIM-3, this regulation happens when PCH-2 is on
609 the synaptonemal complex, temporally overlapping with when chromosomes are competent for
610 meiotic recombination (Deshong et al., 2014). When combined with the biochemical analysis
611 that these mutations reduce the affinity of these proteins for their closure motifs (Figure 7),
612 limiting their ability to adopt the closed conformation, the model becomes even more precise:
613 PCH-2's remodeling of the HORMA domains of HTP-3 and HIM-3 from closed to unlocked
614 decelerates the events of pairing, synapsis and recombination, destabilizing and proofreading
615 them for meiotic fidelity (Giacopazzi et al., 2020). Given that adoption of the closed
616 conformation by HORMADs often reveals a dimerization motif (Rosenberg & Corbett, 2015), a
617 very attractive but speculative extension to this model is that PCH-2's remodeling of meiotic
618 HORMADs from closed to unbuckled destabilizes protein interactions essential for the events of
619 inter-homolog pairing, synapsis and recombination, deliberately slowing their progress.
620
621 Is this deceleration and proofreading of pairing, synapsis and crossover recombination by PCH-
622 2 conserved in other systems, primarily those that deplete meiotic HORMADs during synapsis?
623 We think so. First, PCH-2's orthologs localize to sites associated with synapsis initiation and
624 recombination in budding yeast and plants (Joshi et al., 2009; Lambing et al., 2015), suggesting
625 a role at these sites. Further, despite PCH-2's depletion or redistribution of meiotic HORMADs
626 from chromosomes upon synapsis in some systems, meiotic HORMADs are not completely
627 removed (Borner et al., 2008; Cuacos et al., 2021; Lambing et al., 2015; Wojtasz et al., 2009),
628 suggesting roles for both meiotic HORMADs and PCH-2 even when chromosomes are
629 synapsed. Given that the gradual implementation of crossover formation partially overlaps with
630 when chromosomes are synapsed in budding yeast, plants and mice (Capilla-Perez et al., 2021;
631 Cole et al., 2012; Joshi, Brown, Bishop, & Borner, 2015; Morgan et al., 2021), we propose that

632 PCH-2's presence on synapsed chromosomes contributes to controlling the number and
633 location of crossovers, as observed in *C. elegans* (Deshong et al., 2014).
634
635 The relationship between PCH-2 and HTP-1 is less clear. Despite the small structural
636 differences between HIM-3 and HTP-1 (Figure 2E) that required some adjustments in how we
637 designed our mutational analysis of HTP-1, we predict that HTP-1^{G97T} also shows a reduced
638 affinity for its closure motifs in both HTP-3 and HIM-3, preferentially residing in its unbuckled
639 conformation. The consequences of this difference in protein function are a significant delay in
640 meiotic progression (Figure 6B) and defects in synapsis, DNA repair and crossover
641 recombination (Figure 5D, 5F, & 5H). Since previous data had implicated HTP-1 in controlling
642 meiotic progression, with indirect effects on synapsis, DNA repair and crossover recombination
643 (Martinez-Perez & Villeneuve, 2005; Silva et al., 2014), we favor the interpretation that the
644 primary defect in *htp-1*^{G97T} mutants is the delay in meiotic progression, with secondary, indirect
645 consequences for synapsis and recombination. Mutation of *pch-2* partially suppresses this
646 defect in meiotic progression (Figure 6B), with little effect on synapsis or recombination (Figure
647 5D & 5H), supporting our interpretation. How might a delay in meiotic progression prevent
648 complete synapsis or the normal completion of recombination? This meiotic delay might
649 maintain a cell cycle state in which the synaptonemal complex and/or recombination
650 intermediates are more labile and subject to turnover, through mechanisms such as post-
651 translational modifications, high chromosome mobility, some other unknown condition or some
652 combination of these conditions. Finally, if we are correct and the increase in unlocked HTP-
653 1^{G97T} is responsible for a meiotic delay, with indirect consequences on synapsis and
654 recombination, our data also suggest that unbuckled or unlocked versions of these proteins may
655 not be functionally inert, unlike open Mad2.
656

657 That mutation of *pch-2* only weakly suppresses the delay in meiotic progression we observe in
658 *htp-1*^{G97T} mutants raises two possibilities: 1) the *htp-1*^{G97T} mutation is too severe to allow us to
659 observe this genetic interaction; or 2) PCH-2 does not directly act on HTP-1 to regulate meiotic
660 progression. How might PCH-2 contribute to the regulation of meiotic progression without
661 directly remodeling HTP-1? Since both HTP-3 and HIM-3 have HTP-1 closure motifs in their C-
662 termini (Kim et al., 2014b), PCH-2's remodeling of HTP-3 and HIM-3 may indirectly result in the
663 removal, and remodeling, of HTP-1, contributing to the regulation of meiotic progression. This
664 possibility is particularly attractive since it explicitly coordinates meiotic progression with the rate
665 of pairing, synapsis and recombination.
666
667 Finally, our work shows that PCH-2's regulation of pairing, synapsis, recombination and meiotic
668 progression are cleanly delegated to the remodeling of different meiotic HORMADs: PCH-2
669 remodels HTP-3 from a closed to an unlocked conformation to decelerate pairing and synapsis,
670 HIM-3 to decelerate crossover recombination and HTP-1, either directly or indirectly, to control
671 meiotic progression. This deceleration allows for proofreading of the homolog interactions that
672 underlie these events and ensure fidelity (Giacopazzi et al., 2020). Similar separation of function
673 has been observed in plants and mice: each have two meiotic HORMADs, only one of which
674 (HORMAD1 in mice, ASY1 in plants), appears to be essential for pairing, synapsis and
675 recombination (Caryl et al., 2000; Daniel et al., 2011; Kogo, Tsutsumi, Ohye, et al., 2012; Shin
676 et al., 2010; Shin, McGuire, & Rajkovic, 2013). In the case of mice, a second HORMAD,
677 HORMAD2, is not required for pairing, synapsis or recombination but is essential for efficient
678 meiotic checkpoint responses (Kogo, Tsutsumi, Inagaki, et al., 2012; Wojtasz et al., 2012). In
679 plants, no role for ASY2 has been reported yet. The separation of function we observe in *C.*
680 *elegans* is slightly different: The three essential meiotic HORMADs have overlapping but distinct
681 roles that nonetheless significantly impact pairing, synapsis and recombination (Couteau et al.,
682 2004; Couteau & Zetka, 2005; Goodyer et al., 2008; Kim et al., 2014b; Martinez-Perez et al.,

683 2008; Martinez-Perez & Villeneuve, 2005). However, it is through their regulation by PCH-2 that
684 their distinct roles become more clear, allowing for the coordination of pairing, synapsis,
685 recombination and meiotic progression. This delegation of tasks, as revealed by their regulation
686 by PCH-2, may also explain why this family has expanded so dramatically in *C. elegans*.
687
688 Another possible contributing factor to the expansion of this family in *C. elegans* is the
689 mechanistic uncoupling of meiotic recombination with synapsis. Mice, budding yeast and plants
690 all rely on the initiation of meiotic recombination (Baudat, Manova, Yuen, Jasin, & Keeney,
691 2000; Giroux, Dresser, & Tiano, 1989; Grelon, Vezon, Gendrot, & Pelletier, 2001; Romanienko
692 & Camerini-Otero, 2000) to promote accurate synapsis. Similarly, all of these organisms have a
693 single essential meiotic HORMAD controlling pairing, synapsis and recombination (Caryl et al.,
694 2000; Daniel et al., 2011; Hollingsworth et al., 1990), suggesting a possible connection between
695 these observations. In contrast to these systems, *C. elegans* does not rely on meiotic
696 recombination for accurate chromosome synapsis (Dernburg et al., 1998), suggesting that the
697 family of meiotic HORMADs may have expanded to accommodate the fact that synapsis and
698 recombination are regulated by two different mechanisms in this system.
699
700 While *C. elegans* is unique in that it has four meiotic HORMADs, three of which are essential,
701 it's formally possible that other systems also have different functional classes of meiotic
702 HORMADs, even when they have a single meiotic HORMAD in their genome. For example, in
703 budding yeast, Hop1 can bind directly to nucleosomal DNA (Heldrich et al., 2022), a closure
704 motif in the axis protein Red1 and closure motifs in Hop1 once it's bound to Red1, producing
705 oligomerization (West et al., 2017). These three different classes of Hop1, potentially defined by
706 the molecular nature of their binding to meiotic chromosomes, may have different effects on the
707 events of meiotic prophase, particularly in terms of their regulation by Pch2, producing a similar
708 delegation of functions as we observe with HTP-3, HIM-3 and HTP-1.

709 Our data shows that the remodeling of meiotic HORMADs by PCH-2 have consequences on the
710 progress, coordination and fidelity of meiotic prophase events. Major questions that arise from
711 this work is how these meiotic HORMADs contribute to the events of pairing, synapsis and
712 crossover recombination? How does HTP-3 molecularly participate in pairing and synapsis?
713 How does HIM-3 promote crossover recombination? And how does HTP-1 control meiotic
714 progression? Future studies focused on understanding how meiotic HORMADs molecularly
715 interact with each other, other axis proteins, and/or additional binding partners will shed new
716 light on how meiotic HORMADs, in collaboration with PCH-2, drive the coordination of meiotic
717 prophase events to promote fidelity and prevent aneuploidy.
718
719 **Materials and Methods**
720
721 **Genetics, Worm strains**
722 The C*. elegans* Bristol N2 strain was used as the wildtype strain throughout this study.
723 The *him-3*^{R93Y}*, htp-1*^{G97A}, *htp-1*^{G97S}*, and htp-1*^{G97T} alleles were generated by CRISPR-Cas9
724 genome editing supplemented with the *dpy-10* co-conversion method (Arribere et al., 2014).
725
726 The following guide RNA sequences were used:
727 *dpy-10* sgRNA: 5'GCU ACC AUA GGC ACC ACG AGG UUU UAG AGC UAU GCU 3'
728 *him-3* sgRNA: 5'CGU GUG UCU UCA ACA UUC GAG UUU UAG AGC UAU GCU 3'
729 *htp-1* sgRNA: 5' UCA ACU ACU UCG AAA UGC UGG UUU UAG AGC UAU GCU 3'
730
731 The following DNA repair oligonucleotide sequences were used:
732 *dpy-10*: 5' CAC TTG AAC TTC AAT ACG GCA AGA TGA GAA TGA CTG GAA ACC GTA CCG
733 CAT GCG GTG CCT ATG GTA GCG GAG CTT CAC ATG GCT TCA GAC CAA CAG CCT AT
734 3'

735

736 *him-3*^{R93Y}: 5' GCA TTC CAG AGC AGT GTT CCT GCC GCA AAG CGT GTG TCT TCA ACA

737 TTT GAC GGA TTG TAC GAT GCG ATT CAA CAA GGC TAT TTG CGA GAG TTC GCA ATC

738 GTG TTC TAC AAG 3'

739

740 *htp-1*^{G97A}: 5' GCT TCA GAA ACC CAC GGT CTA ACC AAA TCG CTC AAC TAC TTC GAA

741 ATG CTG CTG ATG CAA CAA AGG ATG GGT TTC TGA AAG AAG TCT CCC TCG TGA TCA

742 CAA ATA ATG 3'

743

744 *htp-1*^{G97S}: 5' GCT TCA GAA ACC CAC GGT CTA ACC AAA TCG CTC AAC TAC TTC GAA

745 ATG CTT CAG ATG CAA CAA AGG ATG GGT TTC TGA AAG AAG TCT CCC TCG TGA TCA

746 CAA ATA ATG 3'

747

748 *htp-1* ^{G97T}: 5' 5' GCT TCA GAA ACC CAC GGT CTA ACC AAA TCG CTC AAC TAC TTC GAA

749 ATG CTA CAG ATG CAA CAA AGG ATG GGT TTC TGA AAG AAG TCT CCC TCG TGA TCA

750 CAA ATA ATG 3'

751

752 For CRISPR/Cs9 gene editing, all mutations were made in the N2 wildtype strain. sgRNAs and

753 oligo repair templates were synthesized by Integrated DNA technologies (IDT, Coraville, IA)

754 Injection mixes contained either *htp-1* or *him-3* sgRNA (100 μM final), *dpy-10* sgRNA (100 μM

755 final, (Arribere et al., 2014)), tracrRNA (100 μM final, IDT), purified Cas9 protein (40 μM final),

756 *htp-3* or *him-3* DNA repair oligo (50 μM final, IDT) and *dpy-10* repair oligo (50 μM final, IDT,

757 (Arribere et al., 2014)). Young adults were injected, recovered and stored at either 15 or 20

758 degrees. Roller or *dpy* F1's were singled to individual plates seeded with OP50 and screened

759 for presence of the mutant allele by PCR and BspHI restriction digest (*htp-1)* or RsaI restriction

digest (*him-3*). Individual F2's were then isolated from F1 plates that contained the allele to identify a homozygous strain.

All mutations were verified by sequencing and strains were backcrossed against wildtype worms three times.

Immunofluorescence, Antibodies and Microscopy

Day 1 adult hermaphrodites were dissected 24-28 hours post-late L4 stage and immunostaining and DAPI staining were performed similarly to (Bhalla & Dernburg, 2005). For analyzing bivalents, hermaphrodites were dissected and DAPI stained 48 hours post late L4 stage.

The following primary antibodies were used for this study: rat anti-HIM-8 1:500 (Phillips et al., 2005), guinea pig anti-HTP-3 1:250 (MacQueen et al., 2005), chicken anti-HTP-3 1:250 (MacQueen et al., 2005), rabbit anti-SYP-1 1:500 (MacQueen et al., 2002), guinea pig anti-SYP-1 1:500 (MacQueen et al., 2002), rabbit anti-HTP-1 1:400 (Martinez-Perez et al., 2008), rabbit anti-RAD-51 1:250 (Novus Biologicals, Littleton, CO), guinea pig anti-DSB-1 1:250 (Stamper et al., 2013), mouse anti-GFP 1:100 (Invitrogen, Waltham, MA) and rabbit anti-PCH-2 1:500 (Deshong et al., 2014).

The following secondaries were used for this study: Alexa 488 anti-guinea pig (Invitrogen), Alexa 488 anti-rabbit (Invitrogen), Alexa 488 anti-mouse (Invitrogen), Cy3 anti-rabbit (Jackson Immunochemicals, West Grove, PA), Cy3 anti-rat (Jackson Immunochemicals), Cy3 anti-guinea pig (Jackson Immunochemicals), and Cy5 anti-chicken (Jackson Immunochemicals). All secondary antibodies were used at a 1:500 dilution.

To visualize meiotic nuclei and bivalents, DAPI was used at a dilution of 1:10,000.

786

787 All images except for those in Figure 10 were acquired using a DeltaVision Personal DV system
788 (Applied Precision) equipped with a 100X N.A. 1.40 oil-immersion objective (Olympus), resulting
789 in an effective XY pixel spacing of 0.064 or 0.040 µm. Three-dimensional image stacks were
790 collected at 0.2-µm Z-spacing and processed by constrained, iterative deconvolution. For
791 structured Illumination microscopy, images were obtained as 125 nm spaced Z stacks, using a
792 100x NA 1.40 objective on a DeltaVison OMX Blaze microscopy system, 3D-reconstructed and
793 corrected for registration using SoftWoRx. Image scaling and analysis were performed using
794 functions in the softWoRx software package. Projections were calculated by a maximum
795 intensity algorithm. Composite images were assembled and some false coloring was performed
796 with ImageJ.

797

798 Whole germline images were assembled in ImageJ as in (Toraason et al., 2021) using pairwise
799 stitching and/or grid collection stitching (Preibisch, Saalfeld, & Tomancak, 2009).
800 Quantification of pairing, synapsis, RAD-51 foci, GFP::COSA-1 foci, and DSB-1 positive nuclei
801 was performed as in (Giacopazzi et al., 2020) with a minimum of three germlines per genotype.
802 To determine statistical significance between genotypes, Fisher's exact tests were performed.

803

804 **Protein Expression and Purification**

805

806 The full-length HIM-3 gene (residues 2-291) was PCR-amplified from a *C. elegans* cDNA library
807 and cloned into UC Berkeley Macrolab vector 2-CT (Addgene #29706), which encodes a TEV
808 protease-cleavable His_6-MBP (maltose binding protein) tag. PCR-based mutagenesis was used
809 to generate the R93Y mutant construct. Proteins were expressed in *E. coli* strain Rosetta2
810 pLysS (EMD Millipore) at 20°C for 16 hours, then harvested by centrifugation. Proteins were
811 purified using Ni^{2+} affinity chromatography (HisTrap HP, Cytiva), followed by TEV protease

812 treatment (Tropea, Cherry, & Waugh, 2009) for 48 hours. The cleaved mixture was passed
813 through Ni^{2+} affinity resin a second time to remove uncleaved protein, free His_6-MBP tags, and
814 His_6-tagged TEV protease, and the flow-through was concentrated and further purified by size
815 exclusion chromatography (Superdex 200; Cytiva). Fractions were concentrated by ultrafiltration
816 (Amicon Ultra, EMD Millipore), aliquoted, and stored at -80°C.
817
818
819 **Fluorescence polarization binding assays**
820 N-terminal FITC-Ahx labeled peptides were synthesized (BioMatik), resuspended in DMSO,
821 then diluted into binding buffer (20 mM Tris pH 7.5, 300 mM NaCl, 10% glycerol, 1 mM DTT,
822 0.1% NP-40). Fifty µL reactions containing 50 nM peptide plus indicated amounts of HIM-3 (WT
823 or R93Y) protein were incubated 60 minutes at room temperature, then fluorescence
824 polarization was read in 384-well plates using a TECAN Infinite M1000 PRO fluorescence plate
825 reader. All binding curves were done in triplicate. Binding data were analyzed with Graphpad
826 Prism v. 8 using a single-site binding model.
827
828 **ThermoFluor assays**
829 For protein stability measurement by ThermoFluor assay, purified proteins were diluted to 0.1
830 mg/mL in a buffer containing 20 mM Tris-HCl pH 7.5, 300 mM NaCl, 10% glycerol, and 1 mM
831 DTT. 0.5 µL of SPYRO Orange dye (5,000X concentrate; Thermo Fisher Scientific #S6650) was
832 mixed with 49.5 µL protein solution, and the mixture was sealed in an optically clear PCR plate.
833 In a Bio-Rad CFX Connect real-time PCR system, fluorescence was measured in scan mode
834 "FRET" during a 25°-99° temperature ramp (0.5° intervals, 30 second hold per interval). For
835 analysis, the change in fluorescence per step was plotted against temperature, and the peak of

836 this plot (the representing the inflection point in the upward slope of the raw fluorescence curve)
837 was taken as the melting temperature (Tm).
838
839 **Protein crystallization and structure determination**
840 For crystallization, HIM-3(R93Y) was concentrated to 15-20 mg/mL in crystallization buffer (20
841 mM HEPES pH 7.5, 100 mM NaCl, 1 mM DTT) and mixed 1:1 with well solution containing 1.4-
842 1.6 M sodium malonate pH 6.5-7.0. Large crystals grown over the course of two weeks were
843 cryoprotected in 2.5 M (total) sodium malonate and flash-frozen in liquid nitrogen. Diffraction
844 data were collected at the Advanced Light source beamline 8.3.1 (support statement below).
845 Data were indexed and reduced with XDS (Kabsch, 2010), scaled with AIMLESS (Evans &
846 Murshudov, 2013), and converted to structure factors with TRUNCATE (Winn et al., 2011)
847 (**Table S1**). The structure was determined by molecular replacement in PHASER using the
848 structure of HIM-3 (PDB ID 4TRK) (Kim et al., 2014a) as a search model. An initial model was
849 rebuilt in COOT (Emsley, Lohkamp, Scott, & Cowtan, 2010) and refined in phenix.refine (Adams
850 et al., 2010) using positional and individual B-factor (anisotropic for protein atoms, isotropic for
851 water molecules) refinement with riding hydrogens. Structure figures were generated in PyMOL
852 version 2.0 (Schrödinger, LLC).
853
854 **ALS Beamline 8.3.1 support statement**
855 The Berkeley Center for Structural Biology is supported in part by the Howard Hughes Medical
856 Institute. The Advanced Light Source is a Department of Energy Office of Science User Facility
857 under Contract No. DE-AC02-05CH11231. The Pilatus detector on 5.0.1. was funded under NIH
858 grant S10OD021832. The ALS-ENABLE beamlines are supported in part by the National
859 Institutes of Health, National Institute of General Medical Sciences, grant P30 GM124169.
860
861 **<u>Author contributions:</u>**

862 A.E.R., S.G., A.D., K.D.C., and N.B. designed the experiments. A.E.R., S.G., A.D., M.M., V.O.,
863 and K.E. performed the experiments. A.E.R., S.G., A.D., M.M., V.O., K.E., K.D.C., and N.B.
864 analyzed the data. A.E.R and N.B. wrote the initial draft of the manuscript and A.E.R., S.G.,
865 A.D., M.M., V.O., K.E., K.D.C., and N.B. revised the manuscript. K.D.C., and N.B. acquired
866 funding.
867

868 **Acknowledgements:**

869 We would like to thank Abby Dernburg, Monique Zetka and Anne Villeneuve for valuable strains
870 and reagents. We would also like to thank the members of the Bhalla lab as well as Brandt
871 Warecki and Alice Devigne for careful review of the manuscript. This work was supported by the
872 NIH (grant number R35GM141835 [N.B.], T32GM008646 [A.E.R] and R35GM144121 [K.D.C.]).
873 Some strains were provided by the CGC, which is funded by NIH Office of Research
874 Infrastructure Programs (P40 OD010440).
875

876 **References:**

877 Adams, P. D., Afonine, P. V., Bunkóczi, G., Chen, V. B., Davis, I. W., Echols, N., . . . Zwart, P.
878 H. (2010). PHENIX: a comprehensive Python-based system for macromolecular
879 structure solution. *Acta crystallographica Section D, Biological crystallography, 66*, 213-
880 221. doi:10.1107/S0907444909052925

881 Alfieri, C., Chang, L., & Barford, D. (2018). Mechanism for remodelling of the cell cycle
882 checkpoint protein MAD2 by the ATPase TRIP13. *Nature, 559*(7713), 274-278.
883 doi:10.1038/s41586-018-0281-1

884 Aravind, L., & Koonin, E. V. (1998). The HORMA domain: a common structural denominator in
885 mitotic checkpoints, chromosome synapsis and DNA repair. *Trends Biochem Sci, 23*(8),
886 284-286. Retrieved from https://www.ncbi.nlm.nih.gov/pubmed/9757827

887 Arribere, J. A., Bell, R. T., Fu, B. X., Artiles, K. L., Hartman, P. S., & Fire, A. Z. (2014). Efficient
888 marker-free recovery of custom genetic modifications with CRISPR/Cas9 in
889 Caenorhabditis elegans. *Genetics, 198*(3), 837-846. doi:10.1534/genetics.114.169730

890 Baudat, F., Manova, K., Yuen, J. P., Jasin, M., & Keeney, S. (2000). Chromosome synapsis
891 defects and sexually dimorphic meiotic progression in mice lacking Spo11. *Mol Cell,*
892 *6*(5), 989-998. Retrieved from https://www.ncbi.nlm.nih.gov/pubmed/11106739

893 Bhalla, N., & Dernburg, A. F. (2005). A conserved checkpoint monitors meiotic chromosome
894 synapsis in Caenorhabditis elegans. *Science, 310*(5754), 1683-1686.
895 doi:10.1126/science.1117468

896 Bohr, T., Nelson, C. R., Giacopazzi, S., Lamelza, P., & Bhalla, N. (2018). Shugoshin Is
897 Essential for Meiotic Prophase Checkpoints in C. elegans. *Curr Biol, 28*(20), 3199-
898 3211.e3193. doi:10.1016/j.cub.2018.08.026

899 Borner, G. V., Barot, A., & Kleckner, N. (2008). Yeast Pch2 promotes domainal axis
900 organization, timely recombination progression, and arrest of defective recombinosomes
901 during meiosis. *Proc Natl Acad Sci U S A, 105*(9), 3327-3332.
902 doi:10.1073/pnas.0711864105

Capilla-Perez, L., Durand, S., Hurel, A., Lian, Q., Chambon, A., Taochy, C., . . . Mercier, R. (2021). The synaptonemal complex imposes crossover interference and heterochiasmy in Arabidopsis. *Proc Natl Acad Sci U S A, 118*(12). doi:10.1073/pnas.2023613118

Carlton, P. M. (2008). Three-dimensional structured illumination microscopy and its application to chromosome structure. *Chromosome Res, 16*(3), 351-365. doi:10.1007/s10577-008-1231-9

Caryl, A. P., Armstrong, S. J., Jones, G. H., & Franklin, F. C. (2000). A homologue of the yeast HOP1 gene is inactivated in the Arabidopsis meiotic mutant asy1. *Chromosoma, 109*(1-2), 62-71. doi:10.1007/s004120050413

Chen, C., Jomaa, A., Ortega, J., & Alani, E. E. (2014). Pch2 is a hexameric ring ATPase that remodels the chromosome axis protein Hop1. *Proc Natl Acad Sci U S A, 111*(1), E44-53. doi:10.1073/pnas.1310755111

Clairmont, C. S., Sarangi, P., Ponnienselvan, K., Galli, L. D., Csete, I., Moreau, L., . . . D'Andrea, A. D. (2020). TRIP13 regulates DNA repair pathway choice through REV7 conformational change. *Nat Cell Biol, 22*(1), 87-96. doi:10.1038/s41556-019-0442-y

Colaiacovo, M. P., MacQueen, A. J., Martinez-Perez, E., McDonald, K., Adamo, A., La Volpe, A., & Villeneuve, A. M. (2003). Synaptonemal complex assembly in C. elegans is dispensable for loading strand-exchange proteins but critical for proper completion of recombination. *Dev Cell, 5*(3), 463-474. Retrieved from https://www.ncbi.nlm.nih.gov/pubmed/12967565

Cole, F., Kauppi, L., Lange, J., Roig, I., Wang, R., Keeney, S., & Jasin, M. (2012). Homeostatic control of recombination is implemented progressively in mouse meiosis. *Nat Cell Biol, 14*(4), 424-430. doi:10.1038/ncb2451

Couteau, F., Nabeshima, K., Villeneuve, A., & Zetka, M. (2004). A component of C. elegans meiotic chromosome axes at the interface of homolog alignment, synapsis, nuclear reorganization, and recombination. *Curr Biol, 14*(7), 585-592. doi:10.1016/j.cub.2004.03.033

Couteau, F., & Zetka, M. (2005). HTP-1 coordinates synaptonemal complex assembly with homolog alignment during meiosis in C. elegans. *Genes Dev, 19*(22), 2744-2756. doi:10.1101/gad.1348205

Couteau, F., & Zetka, M. (2011). DNA damage during meiosis induces chromatin remodeling and synaptonemal complex disassembly. *Dev Cell, 20*(3), 353-363. doi:10.1016/j.devcel.2011.01.015

Cuacos, M., Lambing, C., Pachon-Penalba, M., Osman, K., Armstrong, S. J., Henderson, I. R., . . . Heckmann, S. (2021). Meiotic chromosome axis remodelling is critical for meiotic recombination in Brassica rapa. *J Exp Bot, 72*(8), 3012-3027. doi:10.1093/jxb/erab035

Daniel, K., Lange, J., Hached, K., Fu, J., Anastassiadis, K., Roig, I., . . . Toth, A. (2011). Meiotic homologue alignment and its quality surveillance are controlled by mouse HORMAD1. *Nat Cell Biol, 13*(5), 599-610. doi:10.1038/ncb2213

942 Dernburg, A. F., McDonald, K., Moulder, G., Barstead, R., Dresser, M., & Villeneuve, A. M.
943 (1998). Meiotic recombination in C. elegans initiates by a conserved mechanism and is
944 dispensable for homologous chromosome synapsis. *Cell, 94*(3), 387-398. Retrieved from
945 https://www.ncbi.nlm.nih.gov/pubmed/9708740

946 Deshong, A. J., Ye, A. L., Lamelza, P., & Bhalla, N. (2014). A quality control mechanism
947 coordinates meiotic prophase events to promote crossover assurance. *PLoS Genet,*
948 *10*(4), e1004291. doi:10.1371/journal.pgen.1004291

949 Emsley, P., Lohkamp, B., Scott, W. G., & Cowtan, K. (2010). Features and development of
950 Coot. *Acta crystallographica Section D, Biological crystallography, 66*, 486-501.
951 doi:10.1107/S0907444910007493

952 Evans, P. R., & Murshudov, G. N. (2013). How good are my data and what is the resolution?
953 *Acta crystallographica Section D, Biological crystallography, 69*, 1204-1214.
954 doi:10.1107/S0907444913000061

955 Fukuda, T., Daniel, K., Wojtasz, L., Toth, A., & Hoog, C. (2010). A novel mammalian HORMA
956 domain-containing protein, HORMAD1, preferentially associates with unsynapsed
957 meiotic chromosomes. *Exp Cell Res, 316*(2), 158-171. doi:10.1016/j.yexcr.2009.08.007

958 Giacopazzi, S., Vong, D., Devigne, A., & Bhalla, N. (2020). PCH-2 collaborates with CMT-1 to
959 proofread meiotic homolog interactions. *PLoS Genet, 16*(7), e1008904.
960 doi:10.1371/journal.pgen.1008904

961 Giroux, C. N., Dresser, M. E., & Tiano, H. F. (1989). Genetic control of chromosome synapsis in
962 yeast meiosis. *Genome, 31*(1), 88-94. Retrieved from
963 https://www.ncbi.nlm.nih.gov/pubmed/2687110

964 Goodyer, W., Kaitna, S., Couteau, F., Ward, J. D., Boulton, S. J., & Zetka, M. (2008). HTP-3
965 links DSB formation with homolog pairing and crossing over during C. elegans meiosis.
966 *Dev Cell, 14*(2), 263-274. doi:10.1016/j.devcel.2007.11.016

967 Grelon, M., Vezon, D., Gendrot, G., & Pelletier, G. (2001). AtSPO11-1 is necessary for efficient
968 meiotic recombination in plants. *EMBO J, 20*(3), 589-600. doi:10.1093/emboj/20.3.589

969 Hassold, T., & Hunt, P. (2001). To err (meiotically) is human: the genesis of human aneuploidy.
970 *Nat Rev Genet, 2*(4), 280-291. doi:10.1038/35066065

971 Heldrich, J., Milano, C. R., Markowitz, T. E., Ur, S. N., Vale-Silva, L. A., Corbett, K. D., &
972 Hochwagen, A. (2022). Two pathways drive meiotic chromosome axis assembly in
973 Saccharomyces cerevisiae. *Nucleic Acids Res, 50*(8), 4545-4556.
974 doi:10.1093/nar/gkac227

975 Herruzo, E., Lago-Maciel, A., Baztan, S., Santos, B., Carballo, J. A., & San-Segundo, P. A.
976 (2021). Pch2 orchestrates the meiotic recombination checkpoint from the cytoplasm.
977 *PLoS Genet, 17*(7), e1009560. doi:10.1371/journal.pgen.1009560

978 Herruzo, E., Ontoso, D., Gonzalez-Arranz, S., Cavero, S., Lechuga, A., & San-Segundo, P. A.
979 (2016). The Pch2 AAA+ ATPase promotes phosphorylation of the Hop1 meiotic

980 checkpoint adaptor in response to synaptonemal complex defects. *Nucleic Acids Res,*
981 *44*(16), 7722-7741. doi:10.1093/nar/gkw506

982 Hollingsworth, N. M., Goetsch, L., & Byers, B. (1990). The HOP1 gene encodes a meiosis-
983 specific component of yeast chromosomes. *Cell, 61*(1), 73-84. Retrieved from
984 https://www.ncbi.nlm.nih.gov/pubmed/2107981

985 Joshi, N., Barot, A., Jamison, C., & Borner, G. V. (2009). Pch2 links chromosome axis
986 remodeling at future crossover sites and crossover distribution during yeast meiosis.
987 *PLoS Genet, 5*(7), e1000557. doi:10.1371/journal.pgen.1000557

988 Joshi, N., Brown, M. S., Bishop, D. K., & Borner, G. V. (2015). Gradual implementation of the
989 meiotic recombination program via checkpoint pathways controlled by global DSB levels.
990 *Mol Cell, 57*(5), 797-811. doi:10.1016/j.molcel.2014.12.027

991 Kabsch, W. (2010). XDS. *Acta crystallographica Section D, Biological crystallography, 66*, 125-
992 132. doi:10.1107/S0907444909047337

993 Kim, Y., Kostow, N., & Dernburg, A. F. (2015). The Chromosome Axis Mediates Feedback
994 Control of CHK-2 to Ensure Crossover Formation in C. elegans. *Dev Cell, 35*(2), 247-
995 261. doi:10.1016/j.devcel.2015.09.021

996 Kim, Y., Rosenberg, S. C., Kugel, C. L., Kostow, N., Rog, O., Davydov, V., . . . Corbett, K. D.
997 (2014a). The chromosome axis controls meiotic events through a hierarchical assembly
998 of HORMA domain proteins. *Developmental Cell, 31*, 487-502.
999 doi:10.1016/j.devcel.2014.09.013

1000 Kim, Y., Rosenberg, S. C., Kugel, C. L., Kostow, N., Rog, O., Davydov, V., . . . Corbett, K. D.
1001 (2014b). The chromosome axis controls meiotic events through a hierarchical assembly
1002 of HORMA domain proteins. *Dev Cell, 31*(4), 487-502. doi:10.1016/j.devcel.2014.09.013

1003 Kogo, H., Tsutsumi, M., Inagaki, H., Ohye, T., Kiyonari, H., & Kurahashi, H. (2012). HORMAD2
1004 is essential for synapsis surveillance during meiotic prophase via the recruitment of ATR
1005 activity. *Genes Cells, 17*(11), 897-912. doi:10.1111/gtc.12005

1006 Kogo, H., Tsutsumi, M., Ohye, T., Inagaki, H., Abe, T., & Kurahashi, H. (2012). HORMAD1-
1007 dependent checkpoint/surveillance mechanism eliminates asynaptic oocytes. *Genes*
1008 *Cells, 17*(6), 439-454. doi:10.1111/j.1365-2443.2012.01600.x

1009 Lambing, C., Osman, K., Nuntasoontorn, K., West, A., Higgins, J. D., Copenhaver, G. P., . . .
1010 Franklin, F. C. (2015). Arabidopsis PCH2 Mediates Meiotic Chromosome Remodeling
1011 and Maturation of Crossovers. *PLoS Genet, 11*(7), e1005372.
1012 doi:10.1371/journal.pgen.1005372

1013 Lorenz, A., Wells, J. L., Pryce, D. W., Novatchkova, M., Eisenhaber, F., McFarlane, R. J., &
1014 Loidl, J. (2004). S. pombe meiotic linear elements contain proteins related to
1015 synaptonemal complex components. *J Cell Sci, 117*(Pt 15), 3343-3351.
1016 doi:10.1242/jcs.01203

1017 MacQueen, A. J., Colaiacovo, M. P., McDonald, K., & Villeneuve, A. M. (2002). Synapsis-
1018 dependent and -independent mechanisms stabilize homolog pairing during meiotic
1019 prophase in C. elegans. *Genes Dev, 16*(18), 2428-2442. Retrieved from

1020 http://www.ncbi.nlm.nih.gov/entrez/query.fcgi?cmd=Retrieve&db=PubMed&dopt=Citation
1021 &list_uids=12231631

1022 MacQueen, A. J., Phillips, C. M., Bhalla, N., Weiser, P., Villeneuve, A. M., & Dernburg, A. F.
1023 (2005). Chromosome sites play dual roles to establish homologous synapsis during
1024 meiosis in C. elegans. *Cell, 123*(6), 1037-1050. doi:10.1016/j.cell.2005.09.034

1025 Martinez-Perez, E., Schvarzstein, M., Barroso, C., Lightfoot, J., Dernburg, A. F., & Villeneuve,
1026 A. M. (2008). Crossovers trigger a remodeling of meiotic chromosome axis composition
1027 that is linked to two-step loss of sister chromatid cohesion. *Genes Dev, 22*(20), 2886-
1028 2901. doi:10.1101/gad.1694108

1029 Martinez-Perez, E., & Villeneuve, A. M. (2005). HTP-1-dependent constraints coordinate
1030 homolog pairing and synapsis and promote chiasma formation during C. elegans
1031 meiosis. *Genes Dev, 19*(22), 2727-2743. doi:10.1101/gad.1338505

1032 Morgan, C., Fozard, J. A., Hartley, M., Henderson, I. R., Bomblies, K., & Howard, M. (2021).
1033 Diffusion-mediated HEI10 coarsening can explain meiotic crossover positioning in
1034 Arabidopsis. *Nat Commun, 12*(1), 4674. doi:10.1038/s41467-021-24827-w

1035 Phillips, C. M., Wong, C., Bhalla, N., Carlton, P. M., Weiser, P., Meneely, P. M., & Dernburg, A.
1036 F. (2005). HIM-8 binds to the X chromosome pairing center and mediates chromosome-
1037 specific meiotic synapsis. *Cell, 123*(6), 1051-1063. doi:10.1016/j.cell.2005.09.035

1038 Preibisch, S., Saalfeld, S., & Tomancak, P. (2009). Globally optimal stitching of tiled 3D
1039 microscopic image acquisitions. *Bioinformatics, 25*(11), 1463-1465.
1040 doi:10.1093/bioinformatics/btp184

1041 Raina, V. B., & Vader, G. (2020a). Homeostatic Control of Meiotic Prophase Checkpoint
1042 Function by Pch2 and Hop1. *Curr Biol*. doi:10.1016/j.cub.2020.08.064

1043 Raina, V. B., & Vader, G. (2020b). Homeostatic Control of Meiotic Prophase Checkpoint
1044 Function by Pch2 and Hop1. *Curr Biol, 30*(22), 4413-4424.e4415.
1045 doi:10.1016/j.cub.2020.08.064

1046 Romanienko, P. J., & Camerini-Otero, R. D. (2000). The mouse Spo11 gene is required for
1047 meiotic chromosome synapsis. *Mol Cell, 6*(5), 975-987. Retrieved from
1048 https://www.ncbi.nlm.nih.gov/pubmed/11106738

1049 Rosenberg, S. C., & Corbett, K. D. (2015). The multifaceted roles of the HORMA domain in
1050 cellular signaling. *J Cell Biol, 211*(4), 745-755. doi:10.1083/jcb.201509076

1051 San-Segundo, P. A., & Roeder, G. S. (1999). Pch2 links chromatin silencing to meiotic
1052 checkpoint control. *Cell, 97*(3), 313-324. Retrieved from
1053 https://www.ncbi.nlm.nih.gov/pubmed/10319812

1054 Severson, A. F., Ling, L., van Zuylen, V., & Meyer, B. J. (2009). The axial element protein HTP-
1055 3 promotes cohesin loading and meiotic axis assembly in C. elegans to implement the
1056 meiotic program of chromosome segregation. *Genes Dev, 23*(15), 1763-1778.
1057 doi:10.1101/gad.1808809

1058 Shin, Y. H., Choi, Y., Erdin, S. U., Yatsenko, S. A., Kloc, M., Yang, F., . . . Rajkovic, A. (2010).
1059 Hormad1 mutation disrupts synaptonemal complex formation, recombination, and
1060 chromosome segregation in mammalian meiosis. *PLoS Genet, 6*(11), e1001190.
1061 doi:10.1371/journal.pgen.1001190

1062 Shin, Y. H., McGuire, M. M., & Rajkovic, A. (2013). Mouse HORMAD1 is a meiosis i checkpoint
1063 protein that modulates DNA double- strand break repair during female meiosis. *Biol*
1064 *Reprod, 89*(2), 29. doi:10.1095/biolreprod.112.106773

1065 Sievers, F., Wilm, A., Dineen, D., Gibson, T. J., Karplus, K., Li, W., . . . Higgins, D. G. (2011).
1066 Fast, scalable generation of high-quality protein multiple sequence alignments using
1067 Clustal Omega. *Mol Syst Biol, 7*, 539. doi:10.1038/msb.2011.75

1068 Silva, N., Ferrandiz, N., Barroso, C., Tognetti, S., Lightfoot, J., Telecan, O., . . . Martinez-Perez,
1069 E. (2014). The fidelity of synaptonemal complex assembly is regulated by a signaling
1070 mechanism that controls early meiotic progression. *Dev Cell, 31*(4), 503-511.
1071 doi:10.1016/j.devcel.2014.10.001

1072 Stamper, E. L., Rodenbusch, S. E., Rosu, S., Ahringer, J., Villeneuve, A. M., & Dernburg, A. F.
1073 (2013). Identification of DSB-1, a protein required for initiation of meiotic recombination
1074 in Caenorhabditis elegans, illuminates a crossover assurance checkpoint. *PLoS Genet,*
1075 *9*(8), e1003679. doi:10.1371/journal.pgen.1003679

1076 Toraason, E., Adler, V. L., Kurhanewicz, N. A., DiNardo, A., Saunders, A. M., Cahoon, C. K., &
1077 Libuda, D. E. (2021). Automated and customizable quantitative image analysis of whole
1078 Caenorhabditis elegans germlines. *Genetics, 217*(3). doi:10.1093/genetics/iyab010

Tropea, J. E., Cherry, S., & Waugh, D. S. (2009). Expression and purification of soluble His(6)-tagged TEV protease. In *Methods in Molecular Biology* (Vol. 498, pp. 297-307). Totowa, NJ: Humana Press.

Ur, S. N., & Corbett, K. D. (2021). Architecture and Dynamics of Meiotic Chromosomes. *Annu Rev Genet, 55*, 497-526. doi:10.1146/annurev-genet-071719-020235

Varadi, M., Anyango, S., Deshpande, M., Nair, S., Natassia, C., Yordanova, G., . . . Velankar, S. (2022). AlphaFold Protein Structure Database: massively expanding the structural coverage of protein-sequence space with high-accuracy models. *Nucleic Acids Res, 50*(D1), D439-D444. doi:10.1093/nar/gkab1061

Villeneuve, A. M. (1994). A cis-acting locus that promotes crossing over between X chromosomes in Caenorhabditis elegans. *Genetics, 136*(3), 887-902. Retrieved from https://www.ncbi.nlm.nih.gov/pubmed/8005443

West, A. M. V., Komives, E. A., & Corbett, K. D. (2017). Conformational dynamics of the Hop1 HORMA domain reveal a common mechanism with the spindle checkpoint protein Mad2. *Nucleic Acids Res*. doi:10.1093/nar/gkx1196

Winn, M. D., Ballard, C. C., Cowtan, K. D., Dodson, E. J., Emsley, P., Evans, P. R., . . . Wilson, K. S. (2011). Overview of the CCP4 suite and current developments. *Acta crystallographica Section D, Biological crystallography, 67*, 235-242. doi:10.1107/S0907444910045749

Wojtasz, L., Cloutier, J. M., Baumann, M., Daniel, K., Varga, J., Fu, J., . . . Toth, A. (2012). Meiotic DNA double-strand breaks and chromosome asynapsis in mice are monitored by distinct HORMAD2-independent and -dependent mechanisms. *Genes Dev, 26*(9), 958-973. doi:10.1101/gad.187559.112

Wojtasz, L., Daniel, K., Roig, I., Bolcun-Filas, E., Xu, H., Boonsanay, V., . . . Toth, A. (2009). Mouse HORMAD1 and HORMAD2, two conserved meiotic chromosomal proteins, are depleted from synapsed chromosome axes with the help of TRIP13 AAA-ATPase. *PLoS Genet, 5*(10), e1000702. doi:10.1371/journal.pgen.1000702

Yang, C., Hu, B., Portheine, S. M., Chuenban, P., & Schnittger, A. (2020). State changes of the HORMA protein ASY1 are mediated by an interplay between its closure motif and PCH2. *Nucleic Acids Res, 48*(20), 11521-11535. doi:10.1093/nar/gkaa527

Ye, Q., Kim, D. H., Dereli, I., Rosenberg, S. C., Hagemann, G., Herzog, F., . . . Corbett, K. D. (2017). The AAA+ ATPase TRIP13 remodels HORMA domains through N-terminal engagement and unfolding. *EMBO J*. doi:10.15252/embj.201797291

Ye, Q., Rosenberg, S. C., Moeller, A., Speir, J. A., Su, T. Y., & Corbett, K. D. (2015). TRIP13 is a protein-remodeling AAA+ ATPase that catalyzes MAD2 conformation switching. *Elife, 4*. doi:10.7554/eLife.07367

Yokoo, R., Zawadzki, K. A., Nabeshima, K., Drake, M., Arur, S., & Villeneuve, A. M. (2012). COSA-1 reveals robust homeostasis and separable licensing and reinforcement steps governing meiotic crossovers. *Cell, 149*(1), 75-87. doi:10.1016/j.cell.2012.01.052

1118 Zetka, M. C., Kawasaki, I., Strome, S., & Muller, F. (1999). Synapsis and chiasma formation in
1119 Caenorhabditis elegans require HIM-3, a meiotic chromosome core component that
1120 functions in chromosome segregation. *Genes Dev, 13*(17), 2258-2270. Retrieved from
1121 http://www.ncbi.nlm.nih.gov/pubmed/10485848
1122
1123
1124
1125
1126
1127
1128
1129 **Figure Legends**
1130
1131 **Figure 1. PCH-2's localization is consistent with remodeling HORMADs on meiotic axes.**
1132 **A.** Cartoon of synaptonemal complex with axial elements made up of meiotic HORMADs and
1133 the central element component, SYP-1. **B.** Structured illumination microscopy (SIM) images of
1134 meiotic nuclei stained with antibodies against PCH-2 (green) and SYP-1 (magenta). Arrows
1135 represent regions of PCH-2 potentially associated with meiotic axes. Scalebar indicates 5
1136 microns.
1137
1138 **Figure 2. HORMA domain structure of meiotic HORMADs in *C. elegans.* A.** Cartoon
1139 depicting protein domains of HTP-3, HIM-3, HTP-1, and HTP-2. HORMA domains and closure
1140 motifs are shown as colored boxes and labeled. Mutations generated by CRISPR/Cas9 are
1141 shown. **B.** Clustal Omega alignment of the HORMA domains of HTP-3, HIM-3, HTP-1, and
1142 HTP-2. Asterisks represent conserved residues, : represents conservative changes and .
1143 represents semi-conservative changes. Red box indicates targeted reside for mutation for each

1144 respective HORMAD. **C.** Structure of the *C. elegans* HTP-3 HORMA domain (pink) bound to a
1145 closure motif (gray), predicted by AlphaFold 2 ((Varadi et al., 2022)). Right panels show the
1146 position of H96. **D.** Overlay of wild-type (gray; PDB ID 4TRK) and R93Y mutant (green/pink) of
1147 *C. elegans* HIM-3. Right panels show the position of residue 93, and show that the overall
1148 HORMA domain structure is not impacted upon mutation of arginine 93 to tyrosine. **E.** View of
1149 the *C. elegans* HTP-1 HORMA domain (PDB ID 4TZQ) equivalent to the close-up panel in (D),
1150 showing the position of residue G97 (yellow spheres), which is partially buried against a
1151 neighboring alpha-helix.
1152
1153 **Figure 3. *htp-3^{H96Y}* suppresses the acceleration of pairing and synapsis but exacerbates**
1154 **defects in DNA repair and crossover formation in *pch-2* mutants. A.** Cartoon depicting
1155 zones for quantification in the *C. elegans* germline. **B.** Meiotic nuclei stained with DAPI
1156 (magenta) and antibody against HIM-8 (green). Scalebar indicates 5 microns. **C.** Quantification
1157 of percent nuclei paired in zones 1-6 for *syp-1* (blue), *pch-2;syp-1* (red), *htp-3^{H96Y};syp-1* (green)
1158 and *pch-2;htp-3^{H96Y};syp*-1 (purple) mutant strains. ** indicates p-value < 0.01. Significance was
1159 assessed using two-tailed Fisher's exact tests. Error bars represent 95% confidence intervals.
1160 **D.** Meiotic nuclei stained with antibodies against SYP-1(magenta) and HTP-3 (green). Arrows
1161 indicates unsynapsed chromosomes. Scalebar indicates 5 microns. **E.** Quantification of percent
1162 nuclei synapsed in zones 1-6 for wildtype (blue), *pch-2* (red), *htp-3^{H96Y}* (green) and *pch-2;htp-*
1163 *3^{H96Y}* (purple) mutant strains. ** indicates p-value < 0.01. Significance was assessed using two-
1164 tailed Fisher's exact tests. Error bars represent 95% confidence intervals. **F.** Quantification of
1165 percent nuclei synapsed in zones 1-6 for *meDf2/*+ (blue), *pch-2;meDf2/*+ (red), *htp-*
1166 *3^{H96Y};meDf2/*+ (green) and *pch-2;htp-3^{H96Y};meDf2/*+ (purple) mutant strains. Error bars represent
1167 95% confidence intervals. **G.** Meiotic nuclei stained with DAPI (magenta) and antibody against
1168 RAD-51 (green). Scalebar indicates 5 microns. **H.** Quantification of number of RAD-51 foci in
1169 zones 1-6 for wildtype (blue), *pch-2* (red), *htp-3^{H96Y}* (green) and *pch-2;htp-3^{H96Y}* (purple) mutant

1170 strains. Error bars represent standard error of the mean (SEM). **I.** Meiotic nuclei stained with
1171 DNA (magenta) and antibody against GFP::COSA-1 (green). Left indicates representative nuclei
1172 with 6 GFP::COSA-1 foci. Right indicates representative nuclei with 5 GFP::COSA-1 foci.
1173 Scalebar indicates 5 microns. **J.** Quantification of percent nuclei with 5 GFP::COSA-1 foci for
1174 wildtype, *pch-2*, *htp-3*^{H96Y}, and *pch-2;htp-3*^{H96Y} mutant strains. ** indicates p-value < 0.01.
1175 Significance was assessed using two-tailed Fisher's exact-tests. Error bars represent 95%
1176 confidence intervals.
1177
1178 **Figure 4. *him-3*^{R93Y} does not suppress the acceleration of pairing, synapsis, or DNA**
1179 **repair, but does suppress defects in crossover formation in *pch-2* mutants. A.** Meiotic
1180 nuclei stained with DAPI (magenta) and antibody against HIM-8 (green). Arrows indicate paired
1181 nuclei. Scalebar indicates 5 microns. **B.** Quantification of percent nuclei paired in zones 1-6 for
1182 *syp-1* (blue), *pch-2;syp-1* (red), *him-3*^{R93Y}*;syp-1* (green) and *pch-2;him-3*^{R93Y}*;syp*-1 (purple)
1183 mutant strains. ** indicates p-value < 0.01. Significance was assessed using two-tailed Fisher's
1184 exact-tests. Error bars represent 95% confidence intervals. **C.** Meiotic nuclei stained with
1185 antibodies against SYP-1(magenta) and HTP-3 (green). Arrow indicates unsynapsed
1186 chromosomes. Scalebar indicates 5 microns. **D.** Quantification of percent nuclei synapsed in
1187 zones 1-6 for wildtype (blue), *pch-2* (red), *him-3*^{R93Y} (green) and *pch-2;him-3*^{R93Y} (purple) mutant
1188 strains. ** indicates p-value < 0.01. Significance was assessed using two-tailed Fisher's exact-
1189 tests. Error bars represent 95% confidence intervals. **E.** Quantification of percent nuclei
1190 synapsed in zones 1-6 for *meDf2/*+ (blue), *pch-2;meDf2/*+ (red), *him-3*^{R93Y}*;meDf2/*+ (green) and
1191 *pch-2;him-3*^{R93Y}*;meDf2/*+ (purple) mutant strains. Error bars represent 95% confidence intervals.
1192 **F.** Meiotic nuclei stained with DAPI (magenta) and antibody against RAD-51 (green). Scalebar
1193 indicates 5 microns. **G.** Quantification of number of RAD-51 foci in zones 1-6 for wildtype (blue),
1194 *pch-2* (red), *him-3*^{R93Y} (green) and *pch-2;him-3*^{R93Y} (purple) mutant strains. Error bars represent
1195 standard error of the mean (SEM). **H.** Meiotic nuclei stained with DNA (magenta) and antibody

1196 against GFP::COSA-1 (green). Left indicates representative nuclei with 6 GFP::COSA-1 foci.
1197 Right indicates representative nuclei with 5 GFP::COSA-1 foci. Scalebar indicates 5 microns. **I.**
1198 Quantification of percent nuclei with 5 GFP::COSA-1 foci for wildtype, *pch-2*, *him-3*^{R93Y}, and
1199 *pch-2;him-3*^{R93Y} mutant strains. * indicates p-value < 0.05. ** indicates p-value < 0.01.
1200 Significance was assessed using two-tailed Fisher's exact-tests. Error bars represent 95%
1201 confidence intervals. **J.** Oocytes stained with DAPI. Left indicates representative oocyte with
1202 zero univalents. Right indicates representative oocyte with univalents (arrows). Scalebar
1203 indicates 5 microns. **K.** Quantification of percent oocytes with univalents for wildtype, *pch-2*,
1204 *him-3*^{R93Y}, and *pch-2;him-3*^{R93Y} mutant strains. Significance was assessed using two-tailed
1205 Fisher's exact tests. Error bars represent 95% confidence intervals.
1206
1207 **Figure 5. *htp-1*^{G97T} does not genetically interact with *pch-2* in the context of pairing,**
1208 **synapsis, DNA repair, or crossover formation. A.** Meiotic nuclei stained with DAPI (magenta)
1209 and antibody against HIM-8 (green). Arrows indicate paired nuclei. Scalebar indicates 5
1210 microns. **B.** Quantification of percent nuclei paired in zones 1-6 for *syp-1* (blue), *pch-2;syp-1*
1211 (red), *htp-1*^{G97T}*;syp-1* (green) and *pch-2;htp-1*^{G97T}*;syp*-1 (purple) mutant strains. ** indicates p-
1212 value < 0.01. Error bars represent 95% confidence intervals. **C.** Meiotic nuclei stained with
1213 antibodies against SYP-1(magenta) and HTP-3 (green). Arrow indicates unsynapsed
1214 chromosomes. Scalebar indicates 5 microns. **D.** Quantification of percent nuclei synapsed in
1215 zones 1-6 for wildtype (blue), *pch-2* (red), *htp-1*^{G97T} (green) and *pch-2;htp-1*^{G97T} (purple) mutant
1216 strains. ** indicates p-value < 0.01. Significance was assessed using two-tailed Fisher's exact
1217 tests. Error bars represent 95% confidence intervals. **E.** Meiotic nuclei stained with DAPI
1218 (magenta) and antibody against RAD-51 (green). Scalebar indicates 5 microns. **F.**
1219 Quantification of number of RAD-51 foci in zones 1-6 for wildtype (blue), *pch-2* (red), *htp-1*^{G97T}
1220 (green) and *pch-2;htp-1*^{G97T} (purple) mutant strains. Error bars represent standard error of the
1221 mean (SEM). **G.** Meiotic nuclei stained with DNA (magenta) and antibodies against

1222 GFP::COSA-1 (green). Left indicates representative nuclei with 6 GFP::COSA-1 foci. Right
1223 indicates representative nuclei with 5 GFP::COSA-1 foci. Scalebar insicates 5 microns. **H.**
1224 Quantification of distribution of GFP::COSA-1 foci per nucleus for wildtype (blue), *pch-2* (red),
1225 *htp-1*^{G97T} (green) and *pch-2;htp-1*^{G97T} (purple) mutant strains. NS indicates non-significant.
1226 Significance was assessed using two-tailed Student T-test. **E.** Oocytes stained with DAPI. Left
1227 indicates representative oocyte with zero univalents. Right indicates representative oocyte with
1228 univalents (arrows). Scalebar indicates 5 microns. **F.** Quantification of percent oocytes with
1229 univalents for wildtype, *pch-2*, *htp-1*^{G97Y}, and *pch-2;htp-1*^{G97Y} mutant strains. **** indicates p-
1230 value < 0.0001. NS indicates non- significant. Significance was assessed using two-tailed
1231 Fisher's exact tests.
1232
1233 **Figure 6. *htp-1*^{G97T} delays meiotic progression and this delay is partially suppressed by**
1234 **mutation of *pch-2*. A.** Full length representative germlines stained with DAPI (magenta) and
1235 antibody against DSB-1 (green). Scalebar indicates 20 microns. **B.** Quantification of DSB-1
1236 positive meiotic nuclei for wildtype, *htp-1*^{G97A}, *htp-1*^{G97S}, *htp-1*^{G97T} *and pch-2;htp-1*^{G97T} mutant
1237 strains. NS indicates non-significant. ** indicates p-value < 0.01. **** indicates p-value <0.0001.
1238 Statistical significance was assessed using two-tailed Fisher's exact tests. Error bars represent
1239 95% confidence intervals.
1240
1241 **Figure 7. *him-3*^{R93Y} mutants have reduced affinity for closure motifs. A.** Fluorescence
1242 polarization peptide binding assay of HIM-3 (blue) and HIM-3^{R93Y} (green) and measured Kd's. **B.**
1243 Cartoon depicting proposed model for open and closed conformation switching of wildtype HIM-
1244 3 and HIM-3^{R93Y}.
1245
1246 **Figure 8. PCH-2 distributes its regulation of meiotic prophase events by remodeling**
1247 **different meiotic HORMADs.** Cartoon depicting proposed model for PCH-2's regulation of

1248 meiotic prophase events. PCH-2 regulates the progression of pairing and by acting through
1249 HTP-3, crossover recombination through HIM-3, and may regulate meiotic progression through
1250 HTP-1.
1251
1252 **Figure S1. *htp-3^{H96Y}* does not affect meiotic progression. A.** Full length representative
1253 germlines stained with DAPI (magenta) and DSB-1 (green). Scalebar indicates 20 microns. **B.**
1254 Quantification of DSB-1 positive meiotic nuclei for wildtype and *htp-3 ^{H96Y}* mutant strains. NS
1255 indicates non-significant. **C.** Quantification of DSB-1 positive meiotic nuclei for *syp-1* and *htp-3*
1256 *^{H96Y};syp-1* mutants. NS indicates non-significant. Statistical significance was assessed using
1257 two-tailed Fisher's exact tests. Error bars represent 95% confidence intervals.
1258
1259 **Figure S2. *him-3^{R93Y}* localizes to meiotic chromosomes. Top:** Mid-pachytene nuclei from
1260 wildtype and *him-3^{R93Y}* germlines stained with DAPI (magenta) and antibody against HIM-3
1261 (green). **Bottom:** Mid-pachytene nuclei from wildtype and *him-3^{R93Y}* germlines stained with HIM-
1262 3 (white). Scalebar indicates 5 microns.
1263
1264 **Figure S3. *him-3^{R93Y}* does not affect meiotic progression. A.** Full length representative
1265 germlines stained with DAPI (magenta) and antibody against DSB-1 (green). Scalebar indicates
1266 20 microns. **B.** Quantification of DSB-1 positive meiotic nuclei for wildtype and *him-3^{R93Y}* mutant
1267 strains. NS indicates non-significant. **C.** Quantification of DSB-1 positive meiotic nuclei for *syp-1*
1268 and *him-3^{R93Y};syp-1* mutants. NS indicates non-significant. Statistical significance was assessed
1269 using two-tailed Fisher's exact tests.
1270
1271 **Figure S4. *htp-1^{G97T}* localizes to meiotic chromosomes. Top:** Mid-pachytene nuclei from
1272 wildtype and *htp-1^{G97T}* germlines stained with DAPI (magenta) and antibody against HTP-1

1273 (green). **Bottom:** Mid-pachytene nuclei from wildtype and *htp-1*^{G97T} germlines stained with HTP-

1274 1 (white). Scalebar indicates 5 microns.

1275

1276 **Figure S5. HIM3^{R93Y} does not affect HIM-3's protein stability.** Stability curve for purified

1277 wildtype HIM-3 (blue) and HIM-3^{R93Y} (green).

1278

1279 **Table 1. Viability assay and male counts for meiotic HORMAD mutants.** Table with percent

1280 viable progeny and males. Total number of progeny listed in parentheses.

1281

1282 **Table S1. Data collection and refinement statistics.** Table with data collection and

1283 refinement statistics for Figure 7. Explanations of equations listed below the table.

Figure 1

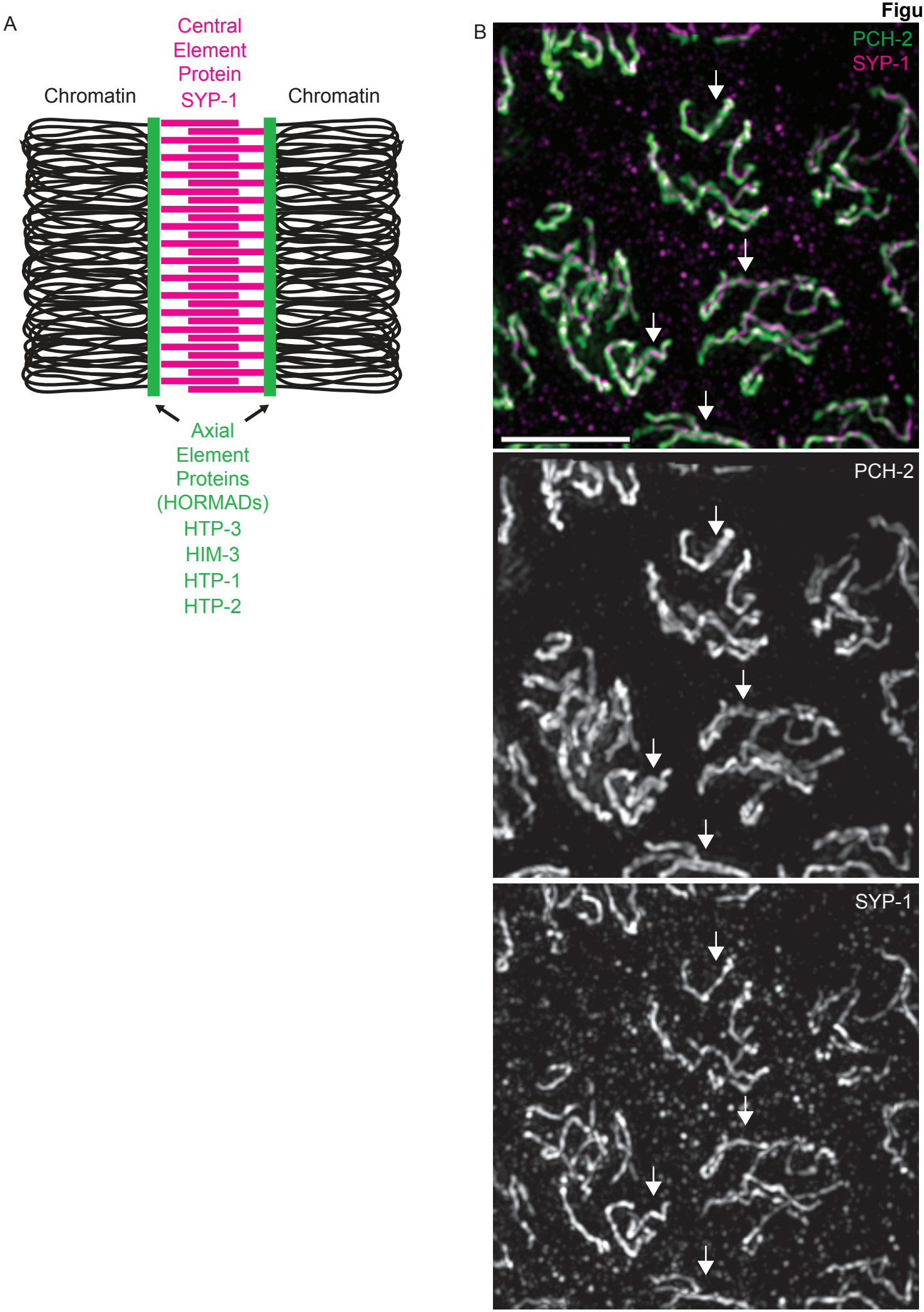
A
Central
Element
Protein
SYP-1
Chromatin
Chromatin
Axial
Element
Proteins
(HORMADs)
HTP-3
HIM-3
HTP-1
HTP-2
B
PCH-2
SYP-1
PCH-2
SYP-1

Figure 2

A

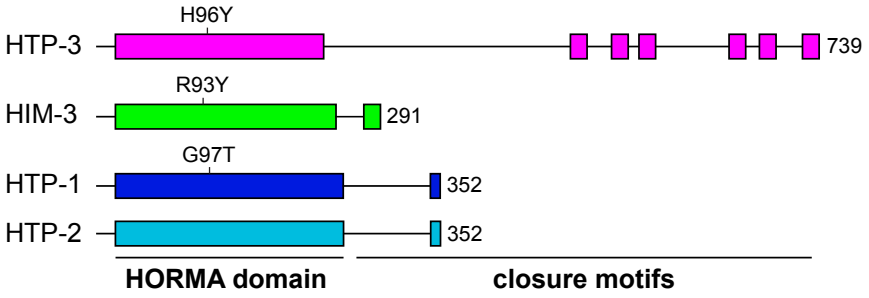

B

```
HTP-3 (57-116) VIPAEYFQDFQVYGDVSGYTLRQDIPEGRSVSSKLLASHDAIRQKLLQKLAIVVEESLN-
HIM-3 (55-114) ILDEKCFKTRTIDKLL-VTAFQSSVPAAKRVSSTFDGLRDAIQQGYLREFAIVFYKKPNE
HTP-1 (59-118) ILGQEYFTKNYITEKLKCMTLCFRNPRSNQIAQLLRNAGDATKDGFLKEVSLVITNNEGD
HTP-2 (59-118) ILEKEYFSKNYITENLSCMTLSFKNLRAHQIAQLLRAAGDATKDGFLKEISLVVTEHDGD
               ::  : *    :   :   ::      .. ::. :    ** ::  *::.::*. :  .
```

C

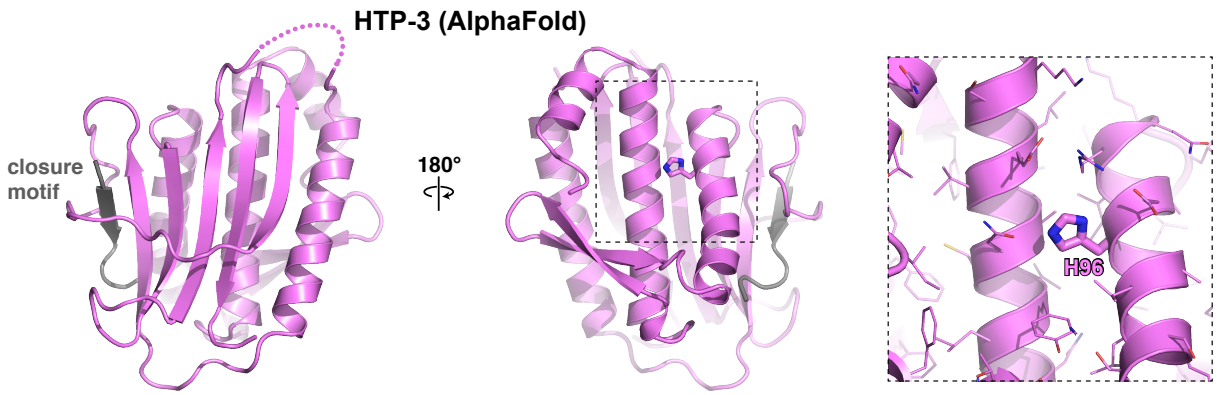

D

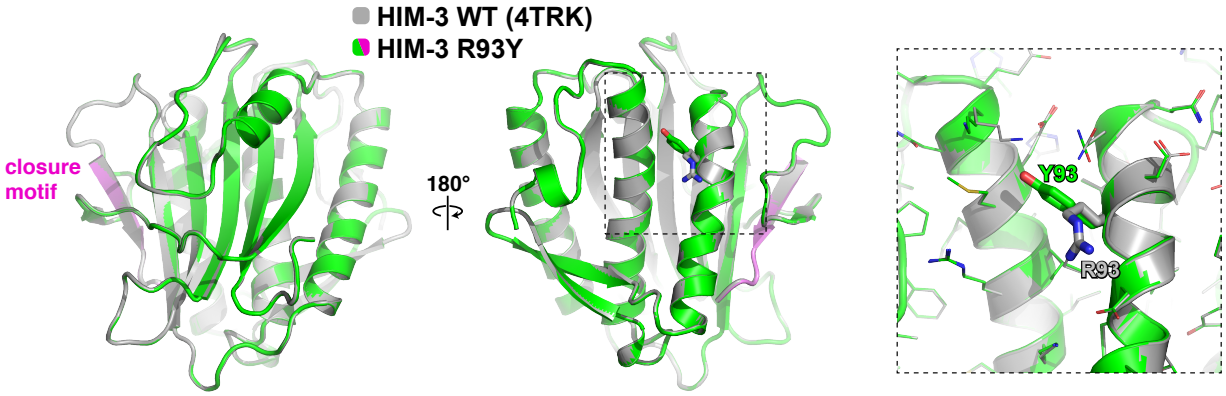

E

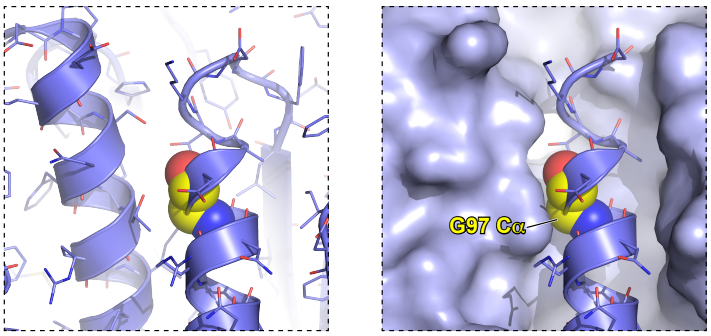

Figure 3

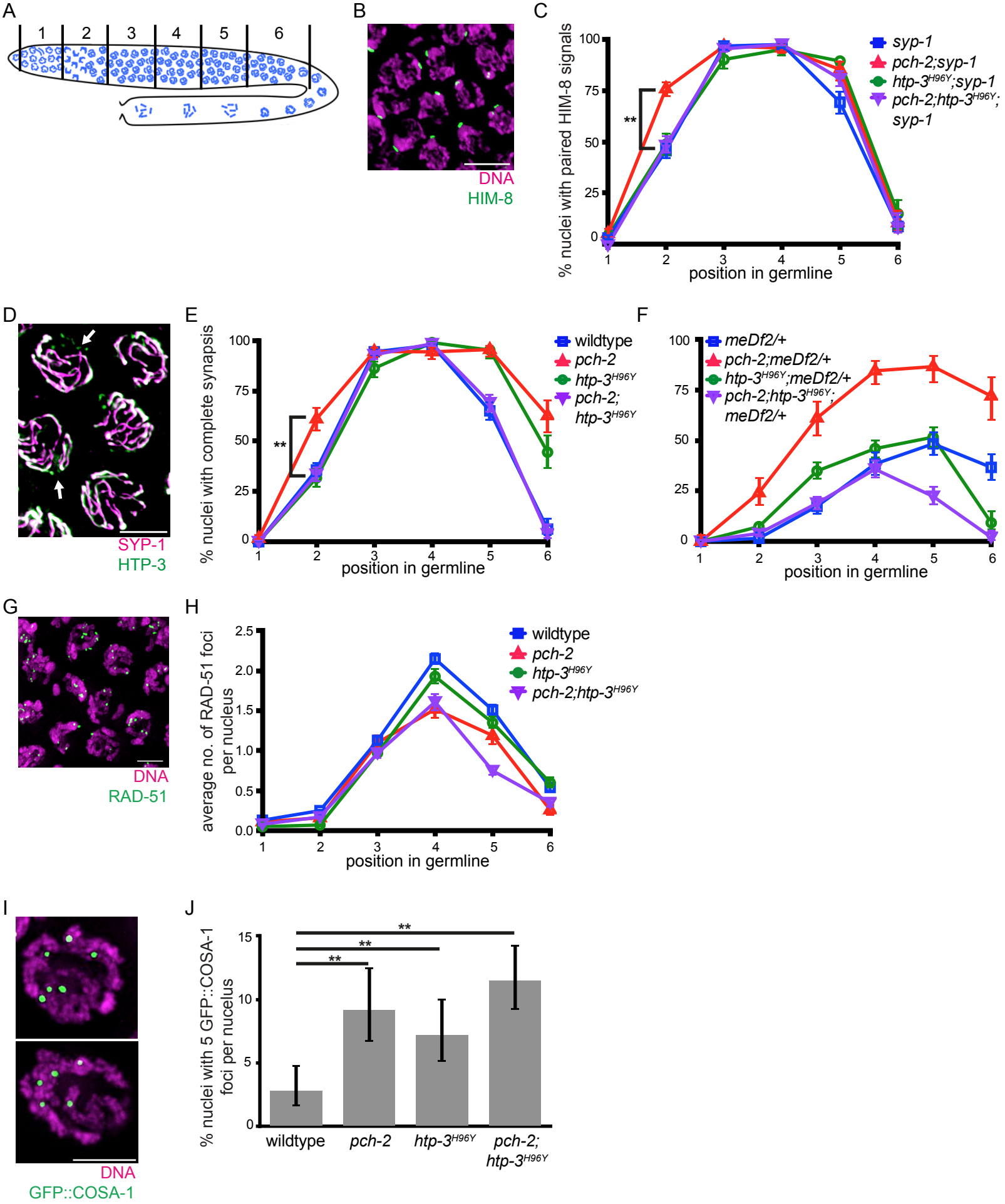
A
1
2
3
4
5
6
B
DNA
HIM-8
C
% nuclei with paired HIM-8 signals
position in germline
syp-1
pch-2;syp-1
htp-3H96Y;syp-1
pch-2;htp-3H96Y;
syp-1
**
D
SYP-1
HTP-3
E
% nuclei with complete synapsis
position in germline
wildtype
pch-2
htp-3H96Y
pch-2;
htp-3H96Y
**
F
meDf2/+
pch-2;meDf2/+
htp-3H96Y;meDf2/+
pch-2;htp-3H96Y;
meDf2/+
position in germline
G
DNA
RAD-51
H
average no. of RAD-51 foci
per nucleus
position in germline
wildtype
pch-2
htp-3H96Y
pch-2;htp-3H96Y
I
DNA
GFP::COSA-1
J
% nuclei with 5 GFP::COSA-1
foci per nucelus
wildtype
pch-2
htp-3H96Y
pch-2;
htp-3H96Y
**
**
**

Figure 4

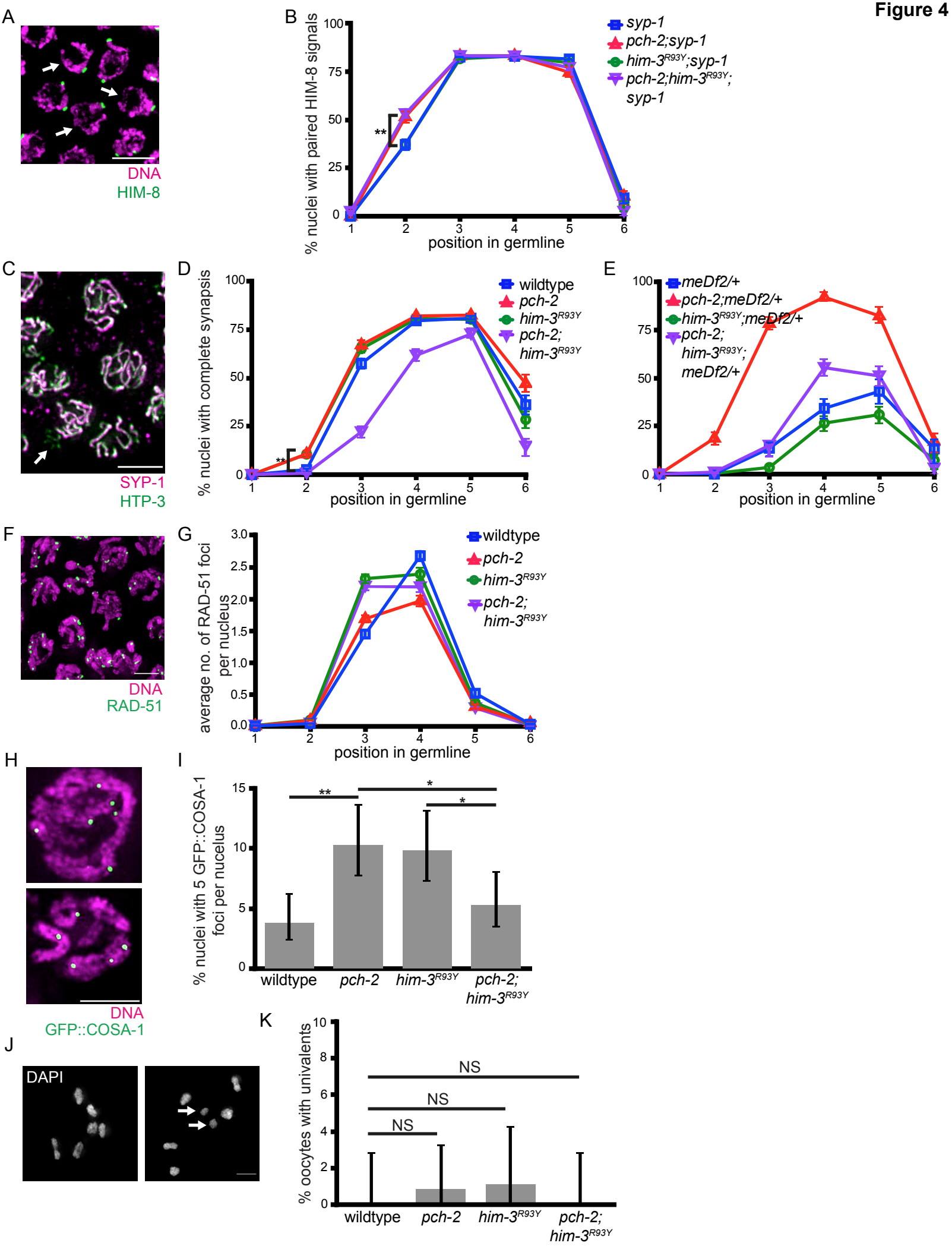
A
DNA
HIM-8
B
% nuclei with paired HIM-8 signals
position in germline
syp-1
pch-2;syp-1
him-3R93Y;syp-1
pch-2;him-3R93Y; syp-1
**
C
SYP-1
HTP-3
D
% nuclei with complete synapsis
position in germline
wildtype
pch-2
him-3R93Y
pch-2; him-3R93Y
**
E
meDf2/+
pch-2;meDf2/+
him-3R93Y;meDf2/+
pch-2; him-3R93Y; meDf2/+
position in germline
F
DNA
RAD-51
G
average no. of RAD-51 foci per nucleus
position in germline
wildtype
pch-2
him-3R93Y
pch-2; him-3R93Y
H
DNA
GFP::COSA-1
I
% nuclei with 5 GFP::COSA-1 foci per nucelus
wildtype
pch-2
him-3R93Y
pch-2; him-3R93Y
**
*
*
J
DAPI
K
% oocytes with univalents
NS
NS
NS
wildtype
pch-2
him-3R93Y
pch-2; him-3R93Y

Figure 5

A

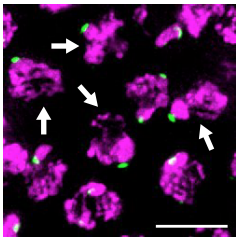

DNA
HIM-8

B

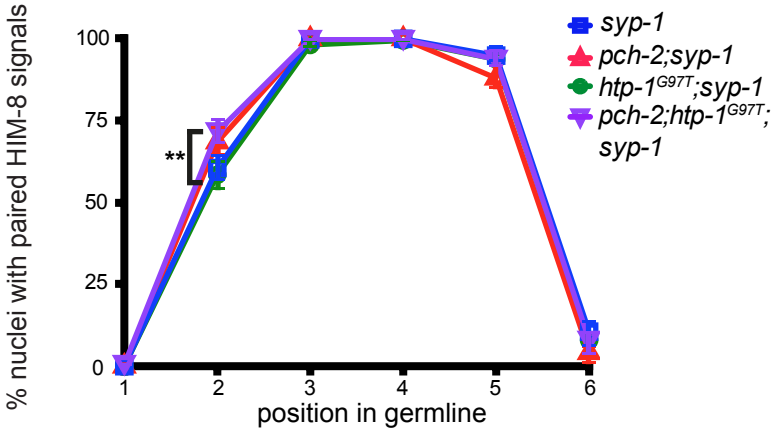

C

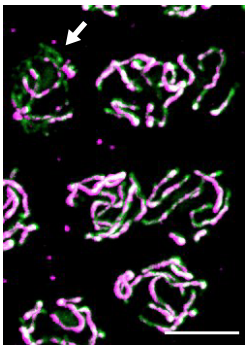

SYP-1
HTP-3

D

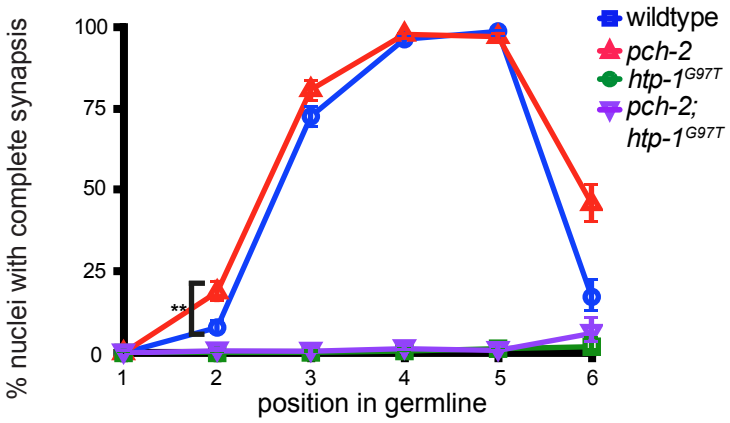

E

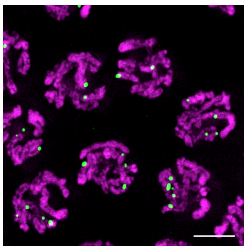

DNA
RAD-51

F

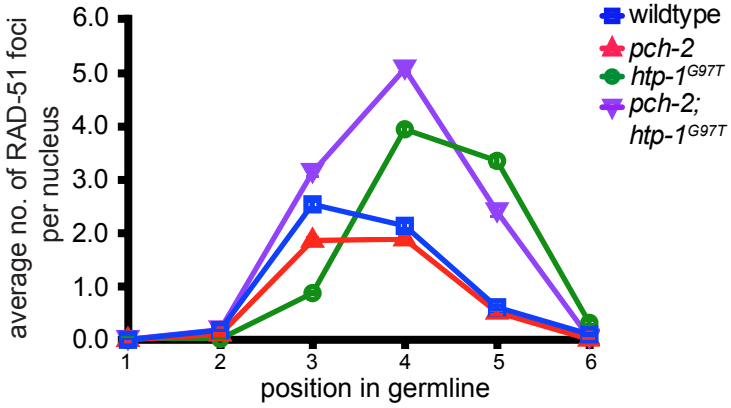

G

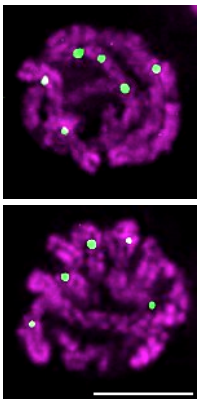

DNA
GFP::COSA-1

H

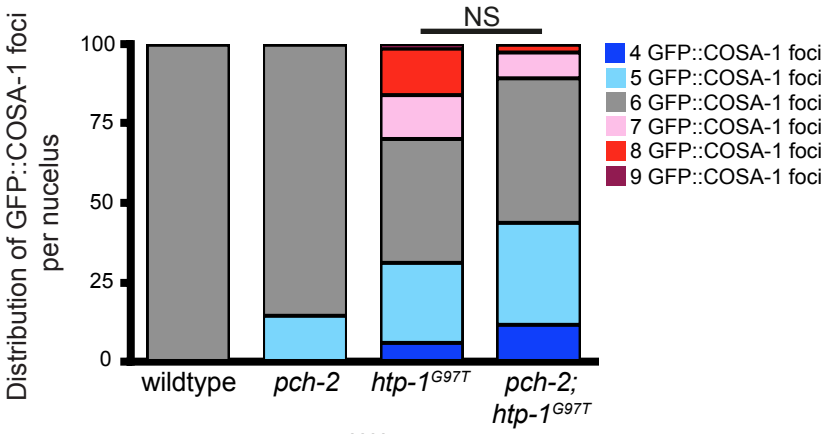

I

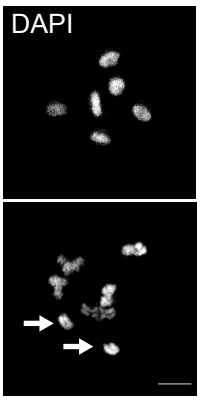

J

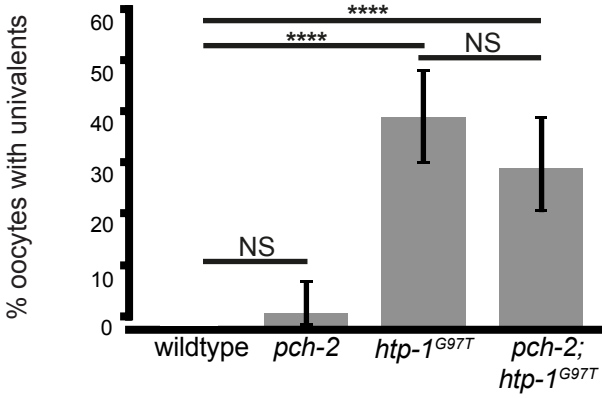

Figure 6

A

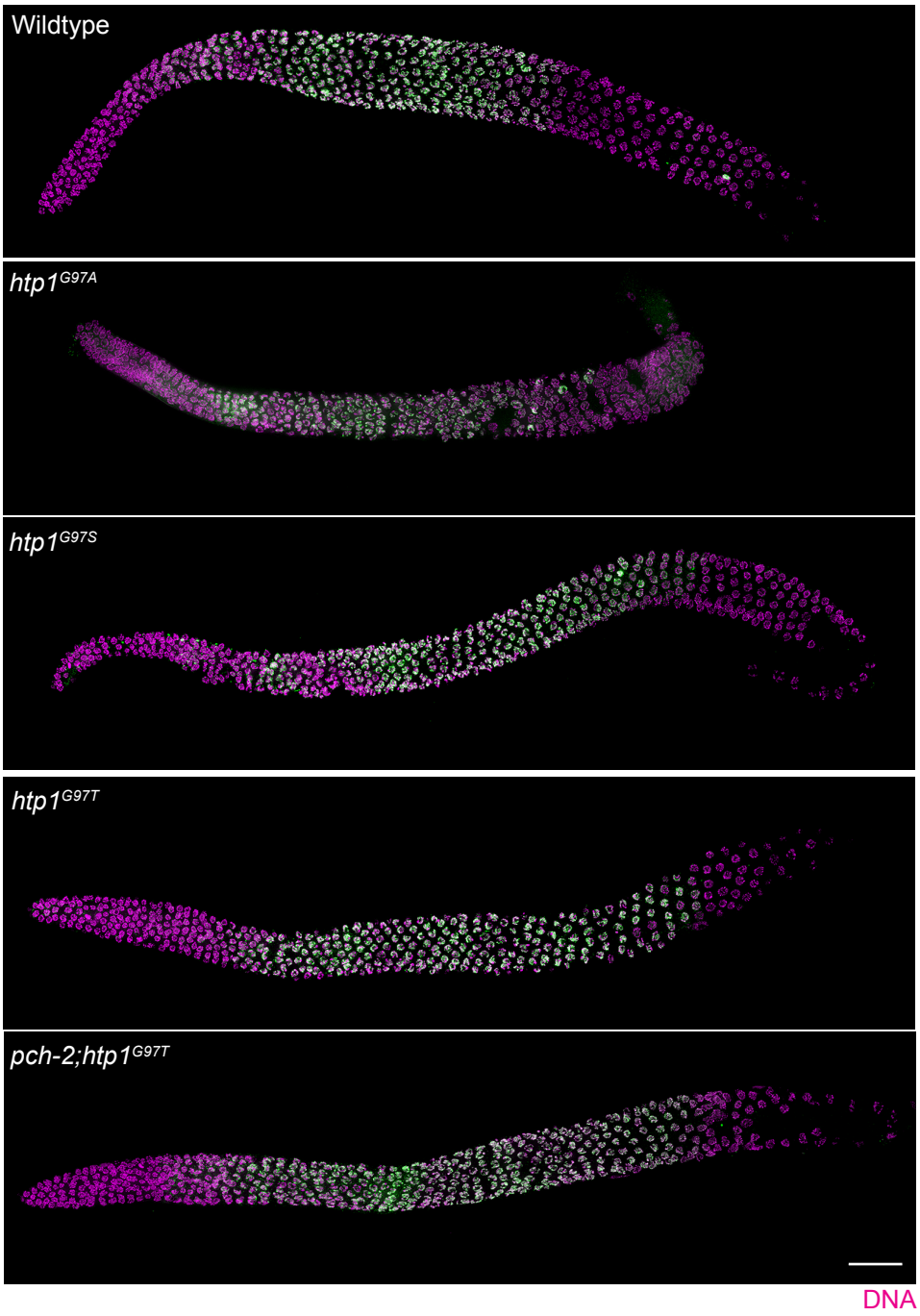
Wildtype
htp1G97A
htp1G97S
htp1G97T
pch-2;htp1G97T
DNA
DSB-1

B

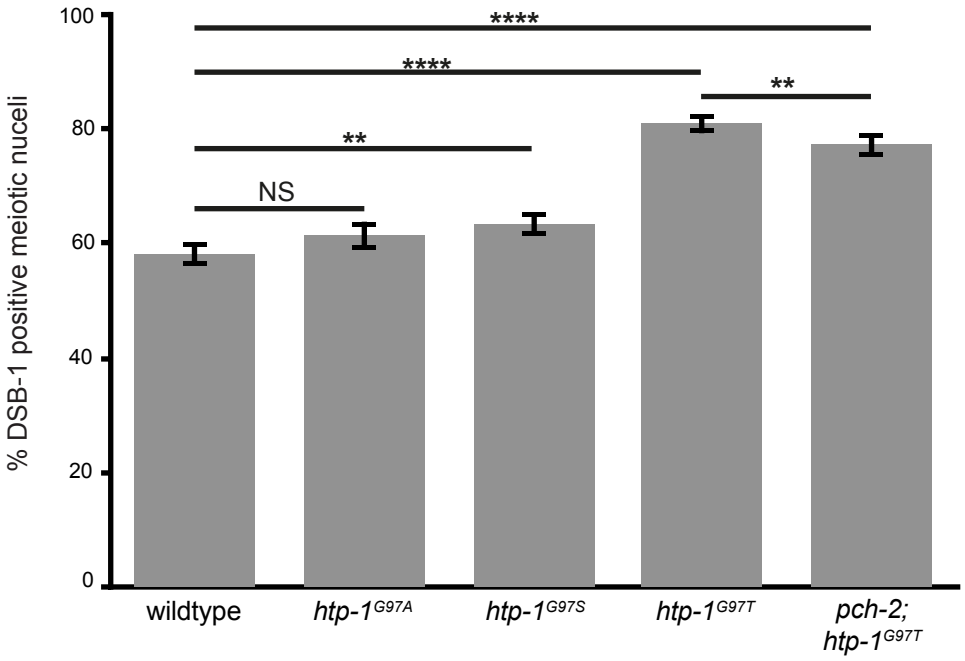
% DSB-1 positive meiotic nuceli
100
80
60
40
20
0
****
****
**
**
NS
wildtype
htp-1G97A
htp-1G97S
htp-1G97T
pch-2;
htp-1G97T

Figure 7

A

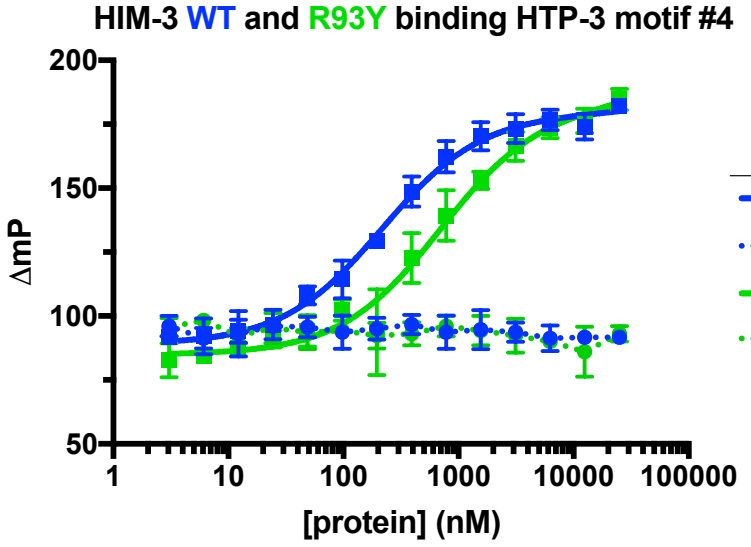

Protein	Peptide	*Kd*
HIM-3^{WT}	HTP-3 motif #4	220 +/- 20 nm
HIM-3^{WT}	Scrambled	*no binding*
HIM-3^{R93Y}	HTP-3 motif #4	690 +/- 130 nm
HIM-3^{R93Y}	Scrambled	*no binding*

B

Figure 8

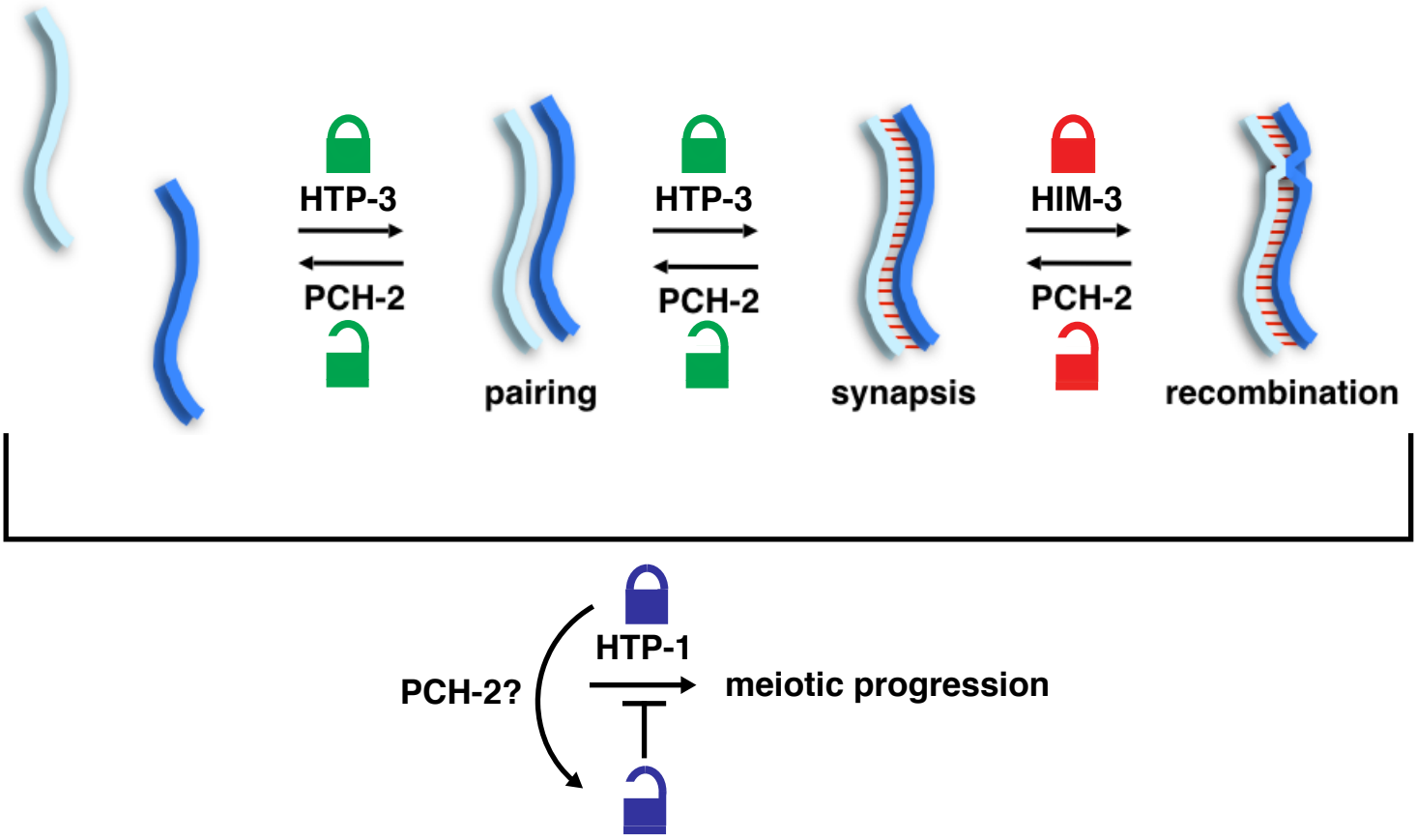
HTP-3
PCH-2
pairing
HTP-3
PCH-2
synapsis
HIM-3
PCH-2
recombination
HTP-1
PCH-2?
meiotic progression

Figure S1

A

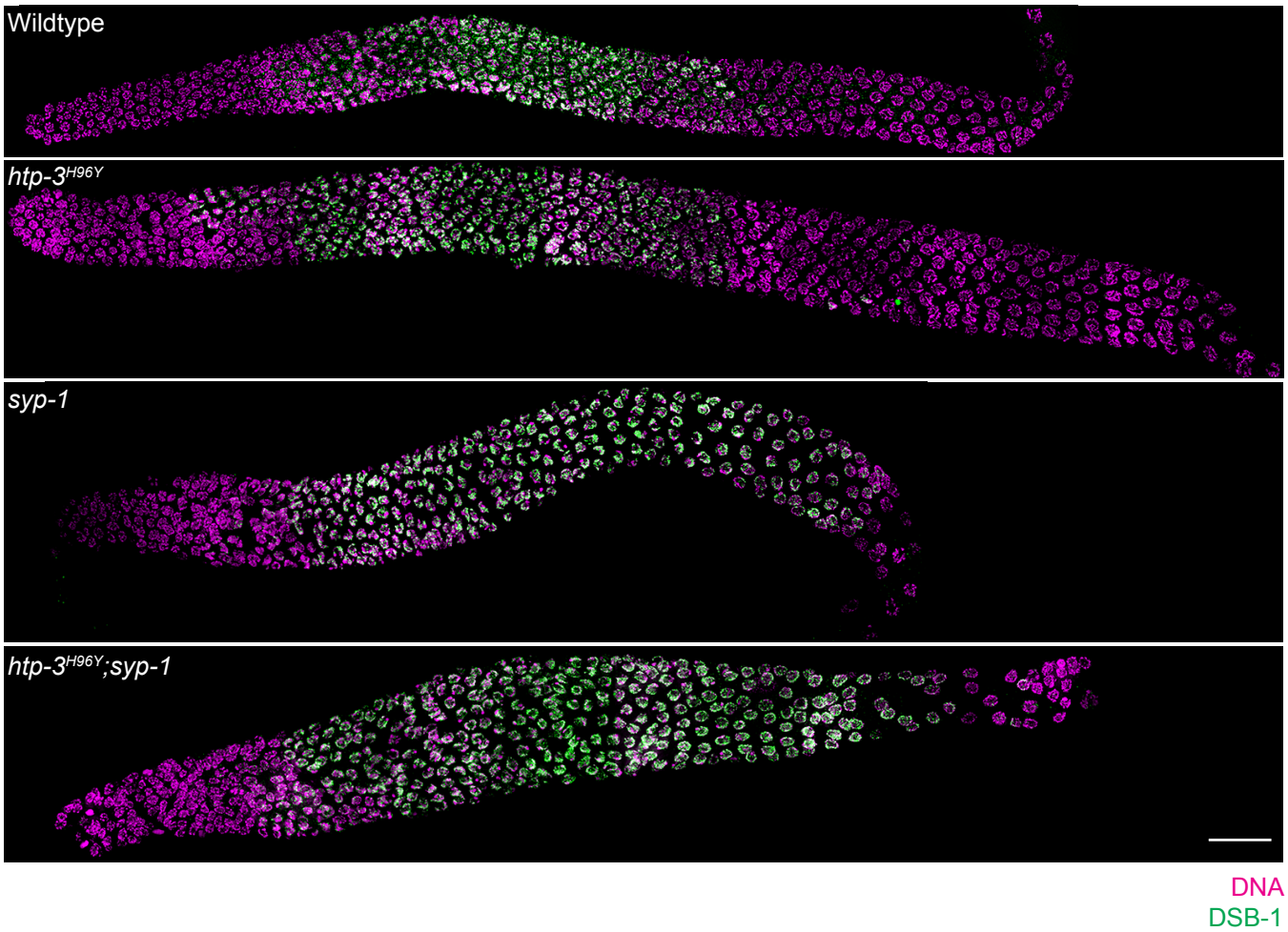

B

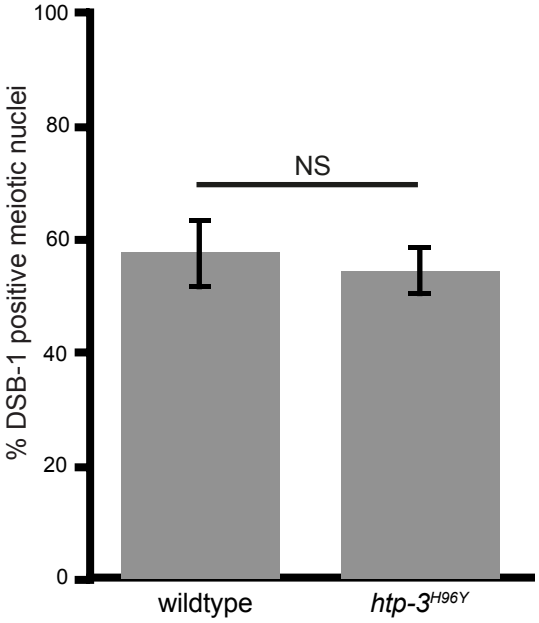

C

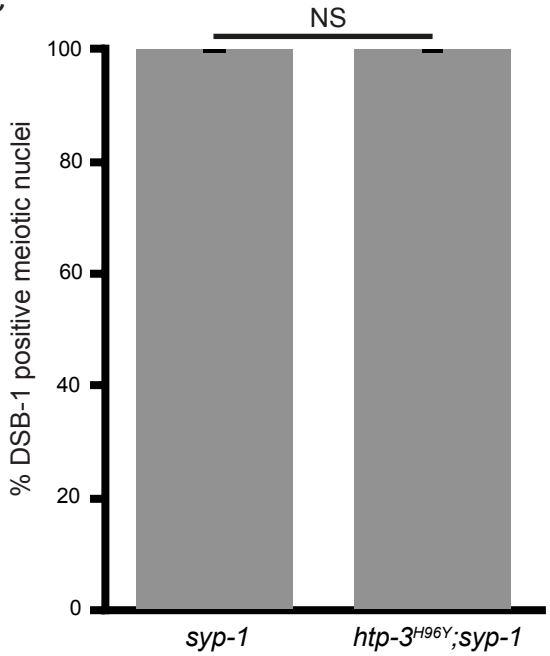

Figure S2

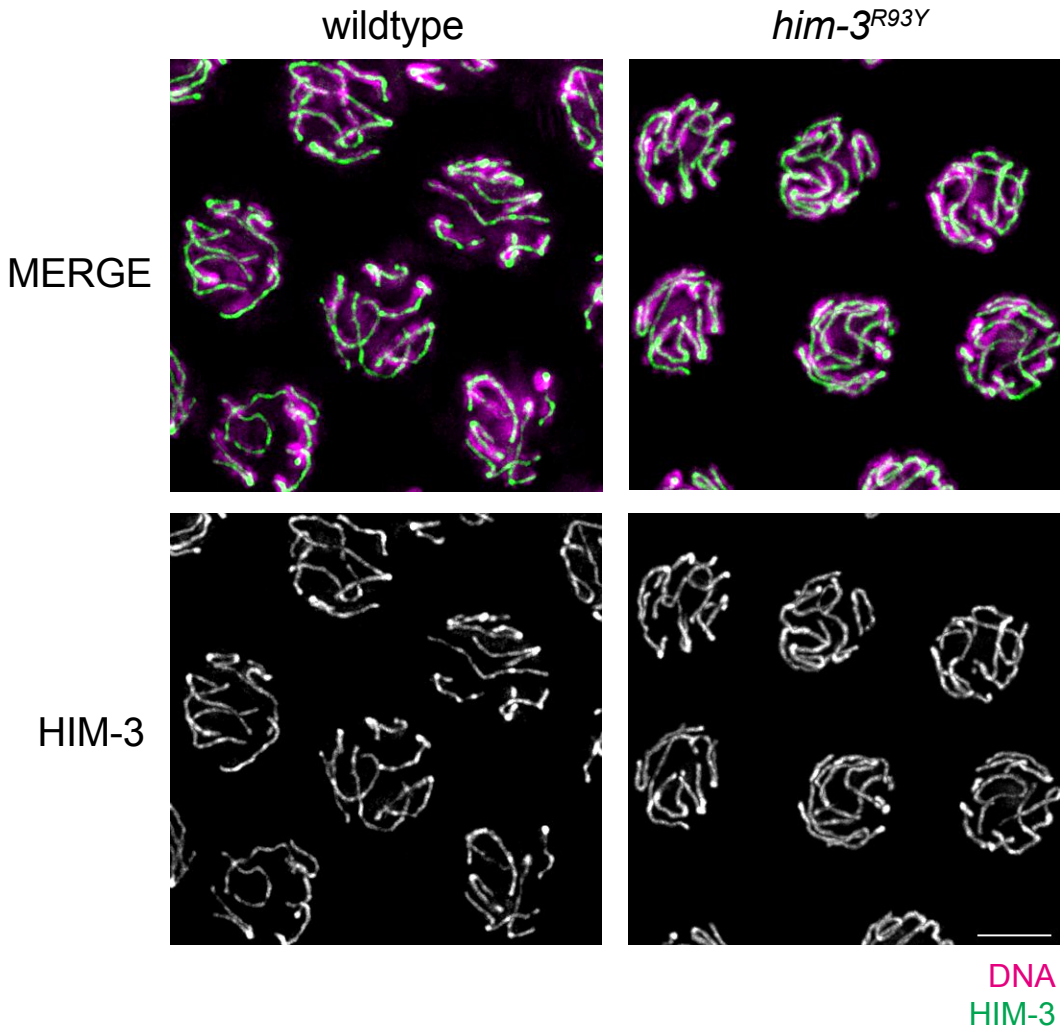

Figure S3

A

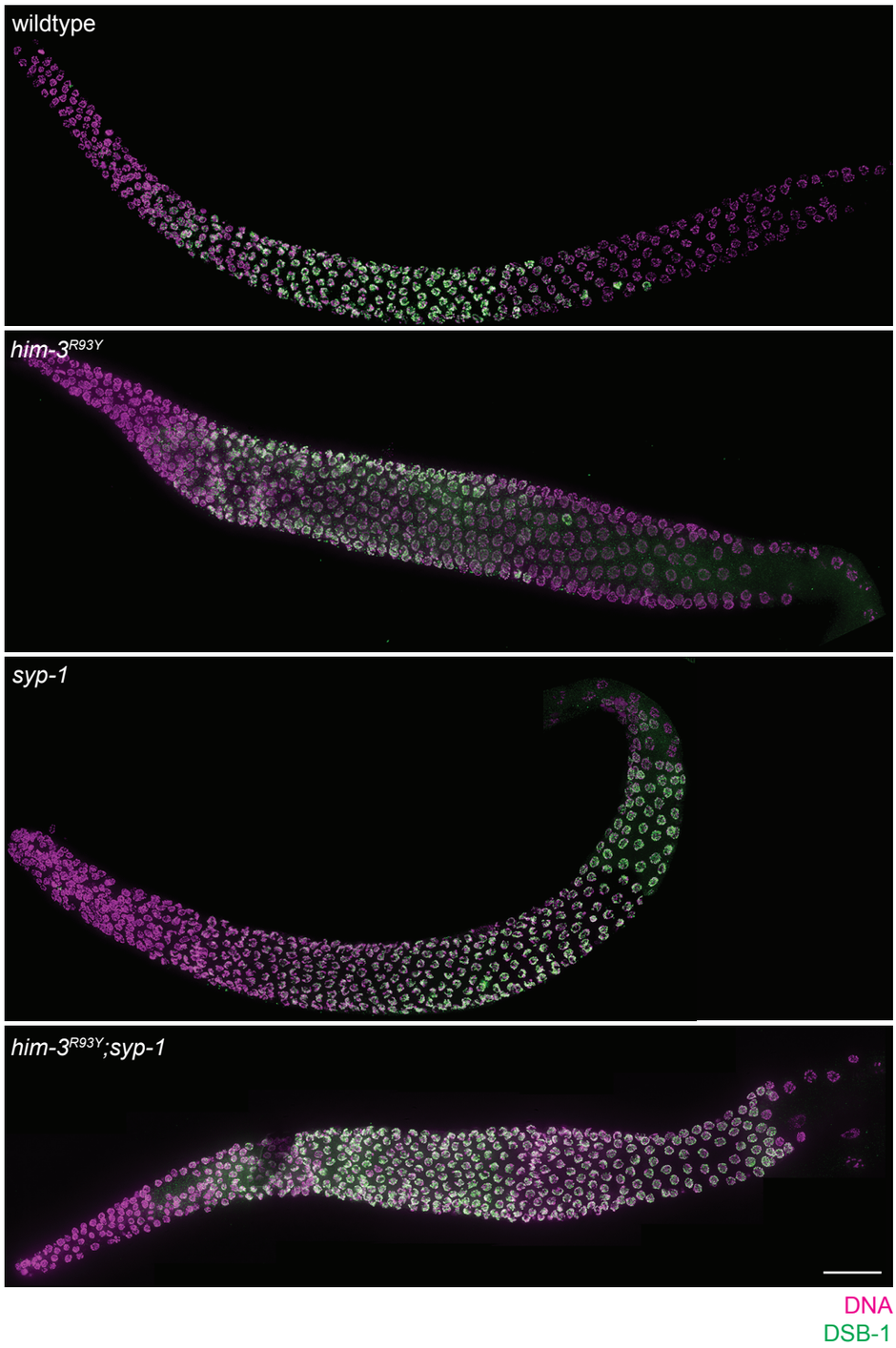

B

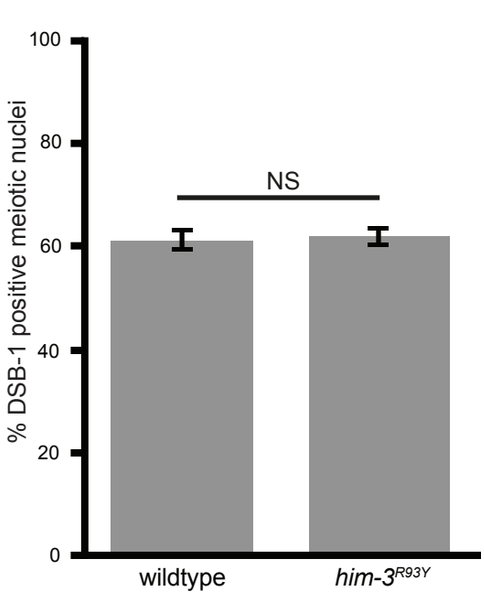

C

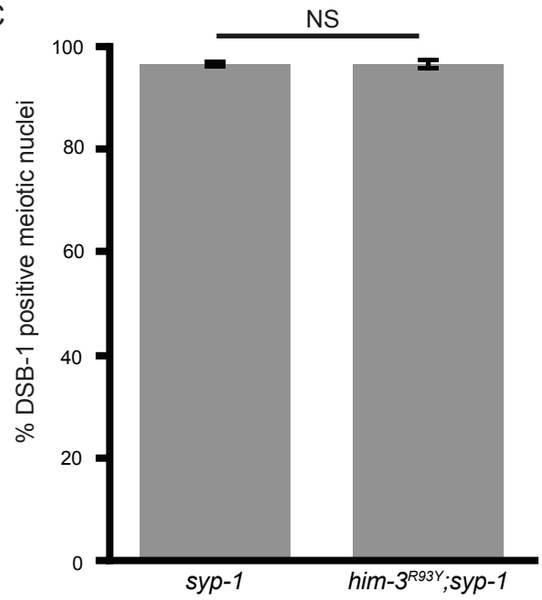

Figure S4

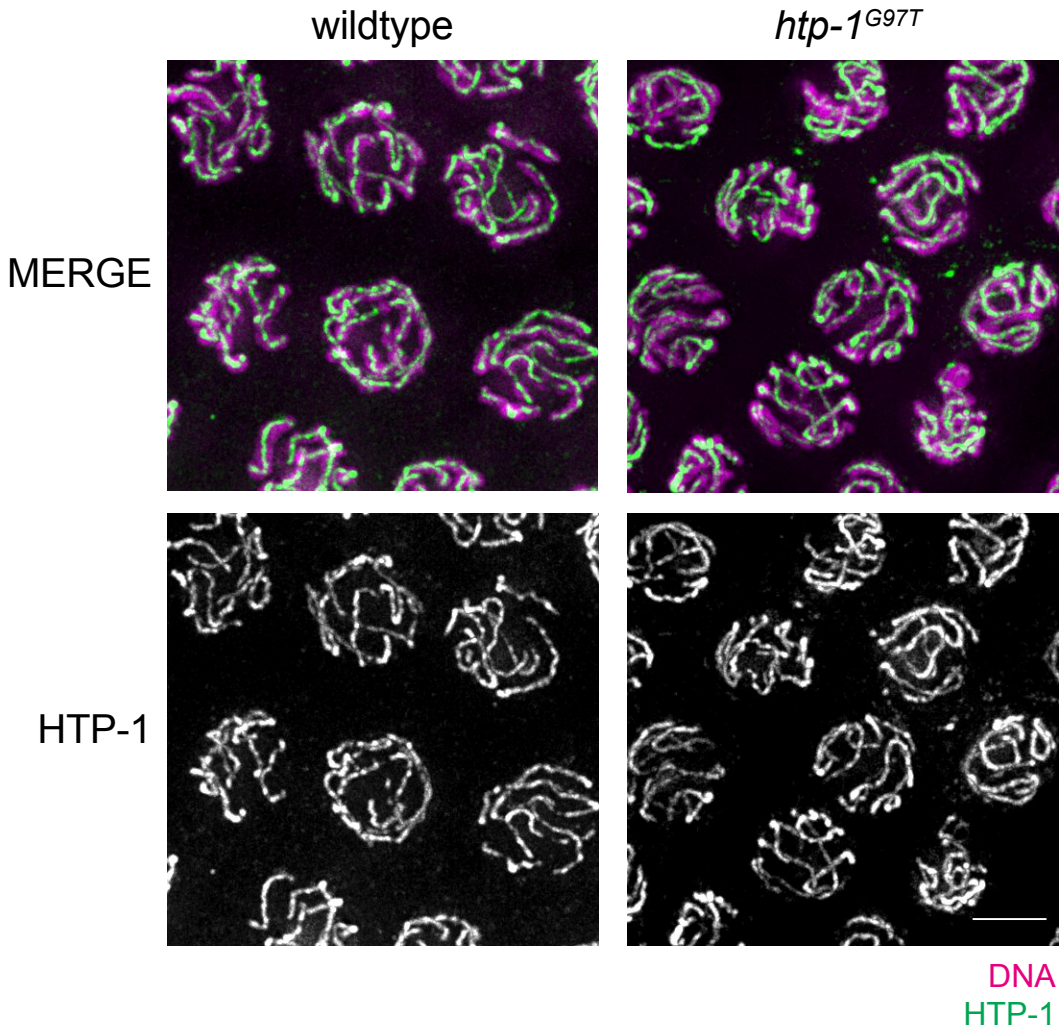

Figure S5

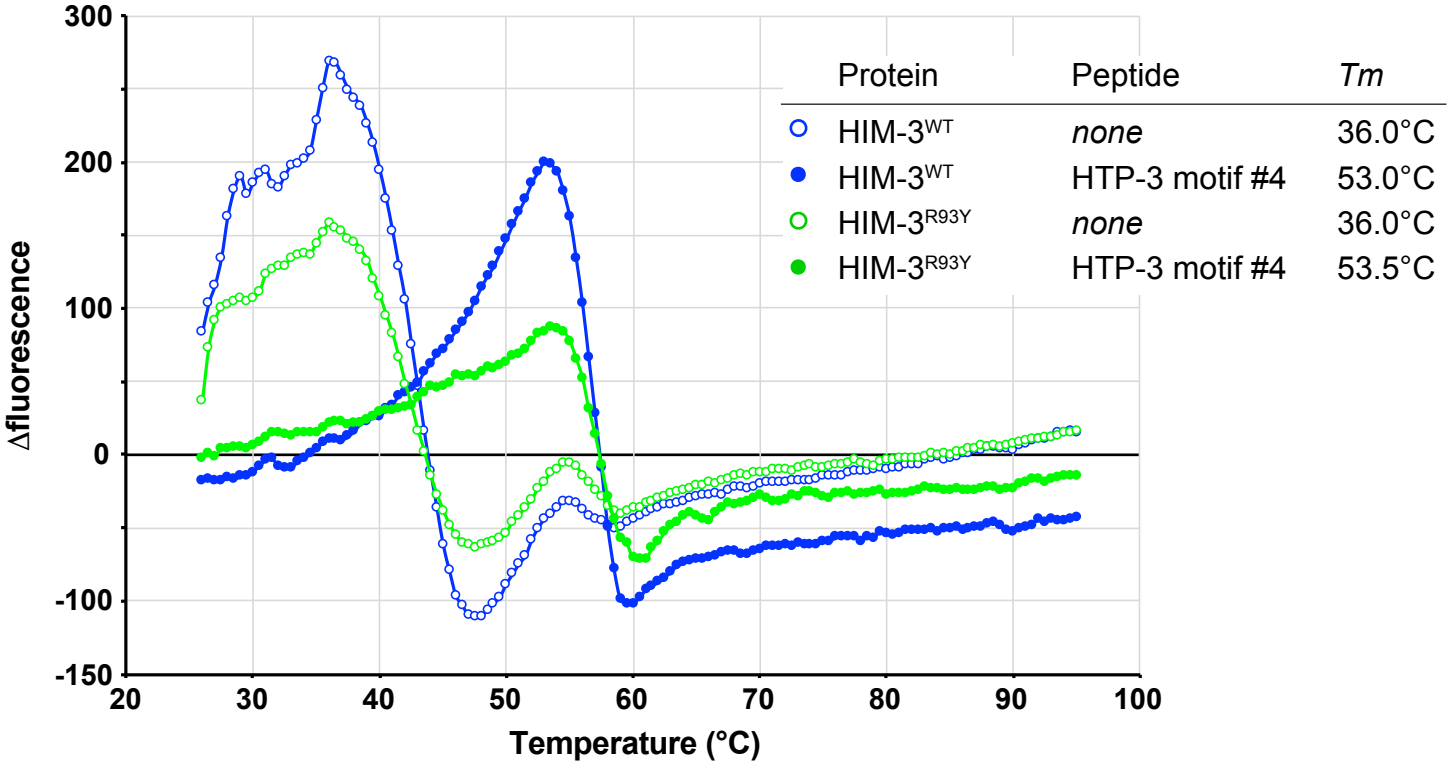
Protein
Peptide
Tm
HIM-3WT
none
36.0°C
HIM-3WT
HTP-3 motif #4
53.0°C
HIM-3R93Y
none
36.0°C
HIM-3R93Y
HTP-3 motif #4
53.5°C
Δfluorescence
Temperature (°C)
300
200
100
0
-100
-150
20
30
40
50
60
70
80
90
100

Table 1: Viability and percent male-self-progeny

genotype	percent viability (total no. of animals)	percent male self-progeny
wildtype	100% (2489)	0.22%
meDf2/+	97% (2286)	10.91%
pch-2	100% (2388)	0.71%
pch-2;meDf2/+	98.15% (1808)	0.83%
htp-3	100% (2586)	0.12%
htp-3;meDf2/+	97.03% (1957)	11.34%
pch-2;htp-3	81.89% (1067)	1.12%
pch-2;htp-3;meDf2/+	83.90% (1652)	10.84%
him-3	100% (3304)	0.15%
him-3;meDf2/+	97.69% (3170)	11.30%
pch-2;him-3	100% (3027)	0.03%
pch-2;him-3;meDf2/+	98.43% (3140)	10.34%
htp-1^{G97T}	67.29% (1984)	2.25%
pch-2;htp-1^{G97T}	58.44% (2175)	1.97%

Table S1. Data collection and refinement statistics

	HIM-3 R93Y
Data collection	
Synchrotron/Beamline	ALS 8.3.1
Date collected	9/14/2018
Resolution (Å)	63.4-1.3
Wavelength (Å)	1.11583
Space Group	$P6_1$
Unit Cell Dimensions (a, b, c) Å	73.23, 73.23, 110.82
Unit cell Angles (α,β,γ) °	90, 90, 120
I/σ (last shell)	27.4
[1]R_{sym} (last shell)	0.055 (2.245)
[2]R_{meas} (last shell)	0.056 (2.081)
[3]$CC_{1/2}$ (last shell)	1 (0.677)
Completeness (last shell) %	100 (100)
Number of reflections	1,632,957
unique	82,280
Multiplicity (last shell)	19.8 (19.7)
Refinement	
Resolution (Å)	63.4-1.3
No. of reflections	82274
working	4255
free	78019
[4]R_{work} (last shell) (%)	14.39 (31.35)
[4]R_{free} (last shell) (%)	16.39 (32.51)
Structure/Stereochemistry	
No. of atoms	4093
solvent	252
hydrogen	1907
r.m.s.d. bond lengths (Å)	0.021
r.m.s.d. bond angles (°)	1.58
Ramachandran favored/allowed (%)	97.03%/100%
Molprobity score	1.55
[5]SBGrid Data Bank ID	8CXK
[6]Protein Data Bank ID	910

[1] $R_{sym} = \sum\sum_j |I_j - \langle I \rangle| / \sum I_j$, where I_j is the intensity measurement for reflection j and $\langle I \rangle$ is the mean intensity for multiply recorded reflections.
[2] $R_{meas} = \sum_h [\sqrt{(n/(n-1))} \sum_j [I_{hj} - \langle I_h \rangle] / \sum_{hj} \langle I_h \rangle$, where I_{hj} is a single intensity measurement for reflection h, $\langle I_h \rangle$ is the average intensity measurement for multiply recorded reflections, and n is the number of observations of reflection h.
[3] $CC_{1/2}$ is the Pearson correlation coefficient between the average measured intensities of two randomly-assigned half-sets of the measurements of each unique reflection.
[4] R_{work}, $R_{free} = \sum||F_{obs}| - |F_{calc}||/|F_{obs}|$, where the working and free R-factors are calculated using the working and free reflection sets, respectively.